NTNU
Norwegian University of
Science and Technology

Shear displacement of a microcalcification in breast tissue

Ulrik Fallrø

Master of Science in Cybernetics and Robotics
Submission date: June 2018
Supervisor: Hans Torp, ITK

Norwegian University of Science and Technology
Department of Engineering Cybernetics

Abstract

Breast cancer is the second largest cause of cancer death for women. Irregular patterns of microcalcifications in the breast may indicate a malignant cancer tumour, which is used as an important indicator in the diagnosis of breast cancer. X-ray mammography is currently the standard for early detection and diagnosis. However, the method is limited due to the high density of connective tissue of the breast. Ultrasound is considered a possible supplement to mammography and has shown abilities in detecting cancer in dense breasts.

The weak signals reflected from microcalcifications in a highly echoic background have proven difficult to detect. The detection of microcalcifications with ultrasound has shown improvements using a dual-band frequency imaging technique named SURF imaging, where findings are confirmed with results from X-ray mammography. SURF imaging is based on a complex pulse consisting of a low frequency (LF) and a high frequency (HF) pulse. The HF to LF ratio is in the range: $7 - 20 : 1$.

By SURF Technology methods for detecting non-linear scattering from microcalcifications are developed. However, it is not yet concluded what makes the microcalcification detectable with SURF imaging. Former studies on shear wave imaging, vibroacoustography, and twinkling sign have shown the radiation force on a microcalcification to be present, but not yet fully understood. In the twinkling sign artifact phenomena the twinkling occurs around or on the surface of a microcalcification. The triggering factor is not concluded, and there may be some parallels to SURF detection. One hypothesis for SURF detection as well as Twinkling Sign Artifact, is ultrasound radiation force inducing oscillating behaviour of a microcalcification making the particle detectable.

This thesis has been aimed at estimating the radiation force effects from a SURF pulse, and simulating the displacement of a microcalcification induced by the force. Addressing these effects can help improve and understand SURF detection of microcalcifications. The simulation tool COMSOL has been utilized for FEM-simulations on the radiation force-induced displacement of a microcalcification. The simulations are performed both for a dynamic case with time-limited pulses transmitted, as well as a stationary case where a pulse is continuously transmitted on the microcalcification. The stationary simulations were performed to find the ultrasound radiation force relation to the Stokes drag force. The shear stiffness in benign and malignant tumours varies widely. An agreement to the Stokes drag force gives an indication on the behaviour of the two tumour types under ultrasound transmission.

Displacement simulations were performed with and without a microcalcification embedded in breast tissue to analyze whether oscillations of the microcalcification is triggering SURF detection. The twinkling sign is also only reported to occur around a microcalcification. The impact from the radiation force from scattering is investigated applying an extra radiation force only on the particle. However, the effect was minimal.

The findings in this thesis provide the conclusion that the radiation force-induced displacement of a microcalcification is not the triggering factor of detection with SURF imaging. The movement of the surrounding tissue dominated the displacement. The simulations have provided a better understanding of the behaviour of a microcalcification under ultrasound transmission. Stationary displacement simulations of breast tissue have shown an agreement with Stokes drag force, a relation not introduced in existing literature. Microbubbles in a crevice or on the surface of microcalcifications are one of the most recently suggested hypotheses for the triggering factor of the Twinkling Sign Artifact. This could also apply to SURF detection. The LF pulse is considered to possibly oscillate the microbubbles, as the resonance frequency of a microbubble is close to the LF frequency for some microbubble sizes. Experiments on a breast mimicking phantom are performed during this semester. Earlier results have been impossible to reproduce. The bubbles may have altered or disappeared. If radiation force-induced displacement of microcalcifications is the triggering factor of detection, the results should be reproducible in experiments.

Sammendrag

Brystkreft er den nest største dødsårsaken blant kreftsyke kvinner. Uregelmessighet av mikrokalker i et bryst kan indikere en ondartet svulst, derfor er tidlige funn av mikrokalker viktig i diagnostisering av brystkreft. I dag er X-ray mammografi vanligst brukt for tidlig diagnostisering og deteksjon. Denne metoden er imidlertid begrenset av høy tetthet av bindevev i brystet. Ultralyd blir sett på som et mulig verdifullt supplement til mammografi.

De svake signalene reflektert fra mikrokalker i vev med ellers høyt ekko har vist seg vanskelige å detektere. Bruk av en to-frekvent ultralydmetode ved navn SURF imaging har gitt gode resultater som samsvarer med bilder fra X-ray mammografi. SURF imaging baseres på en kompleks puls bestående av en lavfrekvent (LF) og en høyfrekvent (HF) puls. Ratioen mellom disse er som regel i området $7 - 20 : 1$.

SURF Technology har produsert metoder og algoritmer for detektering av ulineær spredning fra mikrokalker. Det er imidlertid ikke avklart hva som gjør at en SURF puls detekterer mikrokalk. Studier gjort tidligere på Shear Wave Imaging, Vibroacoustography og Twinkling Sign har vist strålingkraftens tilstedeværelse, men det mangler fremdeles videre undersøkelse av dens faktiske påvirkning på en mikrokalk. I Twinkling Sign Artifact foregår blinkingen kun rundt mikrokalker. Den utløsende faktoren i Twinkling Sign Artifact er ikke bestemt, og det kan trekkes paralleller mellom dens opphav og SURF deteksjon. Hypotese for deteksjon av mikrokalk ved SURF imaging og Twinkling Sign er at strålingskraften fra ultralydpulser setter mikrokalken i oscillasjoner slik at den blir mulig å detektere.

Denne oppgaven har hatt som mål å estimere effektene av indusert strålingskraft fra en SURF puls, og kraften er brukt i simuleringer av kalkpartikkelens forskyvning i et omliggende brystvev. Dette er gjort for å gi forståelse og potensielt forbedre SURF deteksjon av mikrokalker. Verktøyet for simuleringene har vært COMSOL Multiphysics, hvor forskyvning av en mikrokalkpartikkel er simulert i en FEM-modell. Simuleringene er gjort for et reelt tidsbegrenset tilfelle, og for et stasjonært tilfelle med konstant strålingskraft applisert. De stasjonære simuleringene er gjort for å potensielt finne en konvergens med Stokes drag force. Stivheten varierer stort mellom friskt, godartet og ondartet brystvev, og sammenhengen med Stokes gir en indikasjon på hvordan de forskjellige tumortypene beveger seg under ultralyd.

Forskyvingssimuleringene er utført både med og uten en mikrokalk innvevd i brystvevet for å analysere om oscillasjoner av mikrokalken utløser SURF deteksjon. Blinkingen i Twinkling Sign Artifact er kun synlig rundt kalkpartikler. Strålingskraft generert av spredning fra mikrokalk er undersøkt ved at en ekstra kraft kun er anvendt på kalkpartikkelen for å se forskjell i utsving av forskyving. Denne effekten ble observert til å være minimal. Funnene i denne oppgaven har gitt grunner til å konkludere med at forskyving indusert av strålingskraften fra en SURF puls ikke er utslagsgivende for SURF deteksjon av mikrokalk. Utsvinget til forskyvningen viste seg å være dominert av det omliggende vevets bevegelse. Simuleringene i oppgaven har gitt en bredere forståelse av en mikrokalks bevegelse i et vev under ultralyd. Stasjonære forskyvningssimuleringer av et brystvev stemmer overens med

Stokes drag force, denne relasjonen er ikke introdusert før. Den nyest foreslåtte hypotesen omkring Twinkling Sign Artifact er at mikrobobler liggende i en sprekk eller på overflaten av mikrokalken fører til blinking. Dette kan også gjelde for SURF deteksjon. LF pulsen er ansett å muligens oscillere mikroboblen, da resonansfrekvensen til en mikroboble av en viss størrelsesorden er i samme område som LF frekvensen. Eksperimenter har blitt utført på et brystfantom i løpet av semesteret. Tidligere resultater fra eksperimenter har vært nærmest umulige å gjenskape. Boblene kan ha blitt deformert eller forvunnet. Om forskyvning grunnet strålingskraft fra en ultralydpuls er den utløsende faktoren for deteksjon av mikrokalk så burde resultatene fra eksperimenter vært mulige å gjenskape.

Preface

This master thesis has been carried out in Trondheim during the spring of 2018. The project is the final of my Master degree in the engineering program Cybernetics at the Norwegian University of Science and Technology. The work done is developed in cooperation between Department of Engineering Cybernetics (ITK), Department of Circulation and Medical Imaging (ISB) and the private company SURF Technology AS. Professor Emeritus at ISB Bjørn A. J. Angelsen functioned as the external supervisor with Hans Torp at ITK and ISB as the internal supervisor.

In developing simulations in this thesis, Matlab and COMSOL Multiphysics have been used. Experiments were performed by loaning a GE Vivid E9 scanner at ISB and a SURF scanner from NorMIT. During the thesis I have learned how to implement and perform simulations in COMSOL, analysis of results was done with the members of SURF Technology. I have performed the structuring and discussion of the thesis. Theoretical framework is attributed to Bjørn A. J. Angelsen.

Acknowledgement

First, I would like to thank Professor Emeritus Bjørn A. J. Angelsen for supervising me through both my project and master thesis. Also, the team members of SURF Technology deserve great honour. The team includes Stian Solberg, Even Flørenæs and Postdoc Ola Finneng Myhre, who have given me daily guidance as well as including me at a social workplace. Special gratitude also goes to my family and my girlfriend Anine for showing me great support through my years of study. The last year has been tough for me, as my older brother passed away in February the semester I am delivering my master thesis. My supervisors at SURF shown great understanding and kindness, and served me support whenever needed. Without the support from the SURF team, Anine and my family the last months, I would have never been able to deliver my thesis in time.

Contents

Abstract i

Sammendrag iii

Preface v

Acknowledgement v

Table of Contents ix

List of Tables xi

List of Figures xv

Abbreviations xvi

1 Introduction 1
- 1.1 Background and motivation . . . 1
- 1.2 Purpose of study . . . 3
- 1.3 Outline of thesis . . . 4

2 Basic Theory 5
- 2.1 Biomechanics . . . 5
  - 2.1.1 Shear modulus . . . 5
  - 2.1.2 Bulk modulus . . . 6
  - 2.1.3 Poisson ratio . . . 7
- 2.2 Ultrasound physics . . . 7
- 2.3 SURF imaging . . . 10
  - 2.3.1 Pulse Form Distortion . . . 12
- 2.4 Ultrasound radiation force . . . 12
  - 2.4.1 Radiation force from scattering . . . 13
- 2.5 Displacement of a sphere in soft tissue . . . 15

2.5.1 Shear waves in tissue 16
2.5.2 Low frequency fields 18
2.5.3 Low frequency pulsatile URF 20
2.6 Nonlinear elastic quantification 21
2.7 Bubble physics 22

3 Measurement setup 23
3.1 GE Vivid E9-2 23
3.1.1 B-flow imaging 23
3.1.2 9L linear probe 24
3.2 The SURF scanner 24
3.2.1 Vora-II dual-band imaging probe 24
3.3 Multi-modality breast phantom 25

4 Simulation setup 27
4.1 Wavesim 27
4.2 COMSOL 33
4.2.1 Solid mechanics 33
4.2.2 Equation of motion 33
4.2.3 Linear elastic material 34
4.2.4 Body load 35
4.2.5 Initial Values 37
4.2.6 Axial symmetry 38
4.2.7 Low-reflecting boundary 39
4.2.8 Free node 40
4.2.9 Finite Element Analysis 40
4.2.10 Modelling with a Gaussian 41

5 Analysis 43
5.1 Dynamic displacement simulations 43
5.1.1 Dynamic displacements induced by a Gaussian 44
5.1.2 Dynamic displacements induced by a SURF pulse 46
5.1.3 Dynamic displacements induced by three SURF pulses 51
5.1.4 Dynamic displacements induced by three LF pulses 52
5.1.5 Lowering the PRF to trigger oscillations of the microcalcification induced by multiple SURF pulses 53
5.2 Stationary displacement solutions 54
5.3 Effect of varying specific material parameters 58
5.3.1 Varying the shear stiffness of the breast tissue 58
5.3.2 Varying the weight of the microcalcification 60
5.4 Experiments 61
5.5 Discussion 63

6 Conclusion and suggestion of further work 65
6.1 Further work 66

Bibliography **67**

List of Tables

3.1 General transmit parameters of the Vora II probe 24

4.1 Parameters of transmit aperture in Wavesim 28
4.2 Parameters of the chosen medium "Muscle" in pulse simulations 28
4.3 Domain parameters in COMSOL 34

List of Figures

2.1 Shear strain illustration 6
2.2 Illustration of Bulk modulus 6
2.3 Illustration of Poisson ratio 7
2.4 A HF pulse placed on a positive LF pulse. 10
2.5 A HF pulse placed on a negative LF pulse. 11
2.6 Radiation force from scattering 15
2.7 Pressure-flow on a sphere surface 19
2.8 Shear-stress flow on a sphere surface 19
2.9 Calculation of the nonlinear shear modulus 21

3.1 Image of breast phantom used in experiments 25

4.1 Azimuth profile, elevation profile and onaxis pulse profile for a positive SURF pulse generated in Wavesim. 29
4.2 A HF pulse placed on a positive LF pulse with −90° and 90° offsets . . . 30
4.3 The onaxis radiation force induced by a SURF pulse. 30
4.4 Azimuth and elevation radiation force profiles for a SURF pulse 31
4.5 The onaxis radiation force induced by a LF pulse. 32
4.6 Azimuth and elevation radiation force profiles for a LF pulse. 32
4.7 A SURF force profile visualized from the side in COMSOL. 36
4.8 A SURF force profile visualized and zoomed in from above in COMSOL. 36
4.9 A step function controls the body load applied to the microcalcification and tissue domains. 37
4.10 The geometry of a microcalcification embedded in tissue with mesh build. 38
4.11 The geometry zoomed of a microcalcification embedded in breast tissue. . 39
4.12 A Gaussian force profile visualized from the side in COMSOL. 42
4.13 A Gaussian force profile visualized from above in COMSOL. 42

5.1 The displacement of a microcalcification induced by a Gaussian. 44
5.2 The displacement of a homogeneous breast tissue induced by a Gaussian shown together with the microcalcification displacement. 45

5.3 The displacement of a microcalcification with an extra scattering force induced by a Gaussian. 45
5.4 The displacement of a microcalcification induced by a single SURF pulse. 46
5.5 The displacement of homogeneous breast tissue compared to a microcalcification in $(r, z) = (0, 20)$ [mm] induced by a SURF pulse. 47
5.6 The distribution of radiation force on the microcalcification and on the tissue with scattering radiation force besides, both at the axis $r = 0$. . . . 48
5.7 A comparison of the displacement of the microcalcification with and without an added scattering radiation force the first 500 µs. 49
5.8 The displacement in r-direction in tissue-coordinates $(r, z) = (2.5, 20)$ [mm] induced by a SURF pulse. 50
5.9 The displacement in z-direction in tissue-coordinates $(r, z) = (2.5, 20)$ [mm] induced by a SURF pulse. 50
5.10 The displacement induced by three SURF pulses transmitted with a PRF of 14 kHz. The microcalcification is positioned at $(r, z) = (0, 20)$ [mm] and the tissue point is at $(r, z) = (0, 19)$ [mm]. 51
5.11 The displacement of a homogeneous breast tissue at $(r, z) = (0, 20)$ [mm] induced by three SURF pulses transmitted with a PRF of 14 kHz. 52
5.12 The displacement induced by three LF pulses transmitted with a PRF of 14 kHz. The microcalcification is positioned at $(r, z) = (0, 20)$ [mm] and the tissue point is at $(r, z) = (0, 19)$ [mm]. 53
5.13 An oscillating behaviour of a microcalcification is triggered by multiple SURF pulses transmitted with a modified PRF of $\sim$ 5 kHz. 54
5.14 The stationary simulated displacement for a radiation force constantly applied on the microcalcification with MI $= 2$. The calculated displacement by Stokes drag force is the dotted line. 55
5.15 The relative error in simulated stationary displacement compared to the displacement by Stokes drag force for different MIs. 56
5.16 The displacement of a microcalcification pulsed in $t = 220.12$ µs to the stationary solution, the displacement by Stokes drag force is the dotted line. 57
5.17 The stationary displacements for a microcalcification when the shear modulus is varied from 1.2 kPa to 54 kPa with a step of 6.7 kPa. The red line is the calculated displacement by Stokes drag force for increasing shear modulus. 58
5.18 The stationary displacements of a microcalcification when the shear modulus of the surrounding tissue is varied. Time shifting due to increased shear wave velocity is observed. 59
5.19 The stationary displacements of a microcalcification by varying the weight of the particle. 60
5.20 B-flow imaging mode detected three microcalcifications in the breast phantom in January 2018. 61
5.21 The B-flow twinkling experiment from May 2018 detected only one microcalcification. 62
5.22 SURF detection of microcalcifications 62

5.23 Calculated resonance frequency for microbubbles of air with radius of 1 µm to 10 µm and the dotted line is the LF frequency. 64

Abbreviations

SURF = Second order UltRasound Field
NTNU = Norwegian University of Science and Technology
HF = High Frequency
LF = Low Frequency
TA = Twinkling Sign Artifact
ARF = Acoustic Radiation Force
URF = Ultrasound Radiation Force
PRF = Pulse Repetition Frequency
NPD = Nonlinear Propagation Delay
PFD = Pulse Form Distortion
DCS = Delay Corrected Subtraction
FE = Finite Element
FEM = Finite Element Modelling
FEA = Finite Element Analysis
PDE = Partial Differential Equation

Chapter 1

Introduction

1.1 Background and motivation

With an estimate of 44 000 deaths per year, breast cancer is the second largest cause of cancer death for women worldwide[1]. As for finding well-defined factors for developing breast cancer has proven difficult, breast cancer screening of the general women population is important in both early detection and prevention. The screening of breast cancer is today mainly done by X-ray mammography. Breast tissue biopsy confirms irregular masses[2].

X-ray mammography is limited due to the high density of connective tissue of the breast. Compared to mammography, ultrasound imaging is a non-ionizing and less expensive method. The images are also in real-time. However, the trade-off with ultrasound imaging is the limitation of spatial resolution[3].

Microcalcifications are small calcium particles with a diameter of approximately 200 µm, and the particles may be embedded in breast tissues. Irregularities in the distribution of microcalcifications can be an indicator of a malignant tumour[4]. Improving detection of microcalcifications by ultrasound has been a field of study for many years towards diagnosis of breast cancer[5]. The tiny sized particles demand an image of high resolution to be visualised. This has proven difficult, as the echoes from the particles are typically weaker than the echoes from surrounding tissue[6].

A radiation force induced by an ultrasound pulse on tissue generates shear waves, the shear wave imaging technique utilises this. The waves are detected and used to estimate the elastic properties of the tissue. The stress is applied by two ultrasound fields at two different frequencies. Due to the non-linear elasticity of the medium, the two fields generate a radiation force. Shear wave imaging is considered to have good abilities in detecting stiff particles in soft tissue. Microcalcifications have shown to generate a strong shear component[7].

Second order UltRasound Field (SURF) imaging is a dual-band imaging technique invented at the Department of Circulation and Medical Imaging (ISB) at the Norwegian University of Technology (NTNU) in Trondheim in Norway. The method is based on a low frequency (LF) pulse being transmitted simultaneously alongside a high frequency (HF) pulse. The SURF imaging method has provided good results in suppression of multiple reflections of the incident pulse, as well as detection of nonlinear scattering. The method is therefore interesting in the detection of microbubbles and microcalcifications[8]. In the master thesis of Even Flørenæs in the spring of 2017, algorithms were developed detecting microcalcifications in a breast mimicking phantom[9]. However, concluding what triggers the detection of microcalcifications with SURF imaging remains.

When GE Medical System introduced B-flow imaging in 2000[10], this gave a new aspect to the research among microcalcifications in breast tissue. The phenomenon named B-flow Twinkling Sign Artifact (TA) was first reported in 2008[11]. The terminology TA was introduced by Rahmouni as early as in 1996 after experiments utilising Color Doppler mode[12]. The twinkle was seen as alternating colours on Doppler. As the colours in Color Doppler mode represents the direction of the blood flow, the behaviour seen is turbulent blood flow. The artifact typically occurs for strong reflectors such as calculi, microcalcifications and kidney stones[13].

With the twinkling sign as a diagnostic factor in the case of microcalcifications in breast tissue, an increase in specificity and sensitivity of 5% and 39% is reported[11]. Therefore, the twinkling artifact may provide useful information to confirm detection of possible targets. To be able to use the clinical potential of the twinkling sign, it is necessary to address the mechanism behind it. During the discoveries of Twinkling Artifact, several hypotheses of the mechanism behind have been suggested, but the conclusion is yet to be decided.

Three major hypotheses were suggested by Rahmouni[12], including roughness of the scatter surface, phase jitter and micro-oscillation. Although these were suggested for the artifact in Color Flow imaging, the artifact occurs in the same situations in B-flow imaging. Therefore the hypotheses may as well apply for the twinkling in B-flow imaging. The experiments by Liu[14] where done on a phantom with embedded glass beads modelling microcalcifications. For an ultrasound-induced radiation force, an optical system captured the scattered lights to investigate the correlation between B-flow twinkling and oscillation of glass particles. The result indicated that the oscillation of the particles had a close relationship with the occurrence of Twinkling Sign.

Other studies also discuss the radiation force to be the generation of TA. The experiments on the radiation force were examined varying the common parameter Pulse Repetition Frequency (PRF). The study concluded the Acoustic Radiation Force (ARF) to probably not be the triggering factor of TA. However, the study was limited by not being able to study the ARF separately[15]. Another recent hypothesis is that the trapped cavitation microbubbles in a crevice or on the surface of kidney stones are causing the twinkling[16]. There are some physical differences between kidney stones and microcalcifications, but in [17], the study examined the two particles likewise. The struggle with the bubble hypothesis is that no bubbles have yet actually been discovered in a tissue. Twinkling in the experiments performed in a water tank was shown to increase by shrinking and enlarging bubbles, respectively for large sough-surface kidney stones, but this was inadequate for smoother stones. The results support the crevice bubble hypothesis of twinkling and suggest that bubbles on kidney stone crevices giving rise to the twinkling sign artifact may be internal as well as external[16].

In [17], the microbubbles were not considered as the only factor of B-flow twinkling. It was suggested that two factors trigger two unique Doppler Signals, both leading to twinkling. From experiments it was concluded that cavitation bubbles made the twinkling appear. It was also assumed that periodic oscillations of a studied object induced by the acoustic radiation force is another factor of twinkling, but these oscillations were not observed in experiments. The calculi motion was considered to be like the oscillation of a spring pendulum.

Some of the hypotheses for the twinkling sign artifact may as well apply for SURF detection of microcalcifications, which is why the artifact is thorough introduced. Current SURF detection of microcalcifications is based on detecting generated differences in an image, B-flow imaging detects flows. A suggested hypothesis for a microbubble triggering SURF detection is the LF pulse oscillating the bubble making it detectable by the HF pulse. The microbubbles are considered to arise from the air in tissue. Microcalcifications are not detected by transmitting a HF pulse separately, therefore addressing the impact by the LF pulse is interesting.

1.2 Purpose of study

The purpose of this study is to get a better understanding of the behaviour of a microcalcification embedded in breast tissue under ultrasound transmission. The displacement induced by a SURF pulse is investigated to give a further understanding of the manipulation of microcalcifications under SURF transmission. Estimation of the effects in simulations can help provide results in vitro.

In this project, two different simulation tools are utilized. Wavesim is a program developed by SURF technology with user interface is in Matlab. For this project Wavesim is used to calculate and simulate the radiation force generated from a SURF pulse in a breast tissue. The next goal is to have a FEM-model simulating the shear displacement of a microcalcification when a SURF pulse is transmitted. This is done by applying the radiation force generated in Wavesim as a force in simulations of breast tissue in COMSOL. The simulations are firstly tested towards the hypothesis that radiation force-induced displacement is the triggering factor of SURF detection of microcalcifications. The method for investigating this has been to perform displacement simulations with and without a microcalcification embedded in breast tissue. Secondly, the FEM-simulations are performed stationary to evaluate an agreement with an analytic approach of the shear displacement of a microcalcification. This could find a relation to the Stokes drag force and serve a deeper physical insight of the elastic system.

Experiments have been done in vitro on a breast mimicking phantom. Experiments on the B-flow twinkling artifact is performed on a GE Vivid E9-2 scanner. The current SURF algorithm developed in [9] is used on the phantom on a SURF scanner to detect microcalcifications in vitro.

1.3 Outline of thesis

The report will consist of 6 different parts, with one chapter for each part. An outline of the structure is provided below.

Chapter 1 is the introduction with the background, motivation and purpose behind this master thesis.

Chapter 2 includes all the background theory necessary to test hypothesis and analyze results.

Chapter 3 presents the measurement setup used for the experiments performed.

Chapter 4 gives an introduction to the simulation tools and setups used in the research.

Chapter 5 presents and discusses the simulations and experiments within the theoretical framework.

Chapter 6 concludes and summarizes the findings, suggests for further work.

Chapter 2

Basic Theory

This chapter is provided to give an overview of all the necessary basic theory for the research done in this master thesis. This section will begin by describing some basic biomechanics theory, before an introduction of ultrasound physics. After that, the specific ultrasound technique SURF imaging used in this thesis is presented, the benefits of using such a dual-band probe technique are discussed. Further, the calculations of radiation force induced by an ultrasound pulse are explained. This force is inducing the displacements in the breast tissue. The analytic equations for calculating the displacement of a microcalcification sphere embedded in breast tissue under ultrasound radiation force are presented. The theory will after that introduce Nonlinear Elastic Quantification, a relatively new idea describing a Nonlinear Shear Modulus of breast tissue under ultrasound transmission. Lastly, the section will present some bubble theory to understand the physical mechanism by one hypothesis of SURF detection. The theory including ultrasound physics, SURF imaging and ultrasound radiation force is adopted from the project thesis[18], with some adjustments.

2.1 Biomechanics

In the displacement simulations FEM-modelled in COMSOL, some specific material parameters are required. This section is provided to give a brief overview and understanding of the physics behind these parameters, and how the three of them are related.

2.1.1 Shear modulus

Shear modulus is a numerical constant that describes the elasticity of a material under the application of transverse internal forces. The shear modulus is often described as the stiffness of a material. The modulus is defined as the ratio of the shear stress to the shear strain. For a force applied parallel to a surface with area A of a solid material, and an opposing force acting on the opposite face, and a distance l separates the faces, the material will deform a length Δx. The shear modulus is then given by[19]

$$G = \frac{F/A}{\Delta x/l}. \tag{2.1}$$

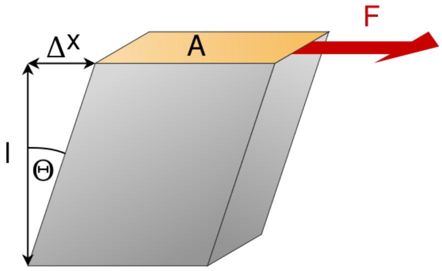

Figure 2.1: An illustration of shear strain[20].

2.1.2 Bulk modulus

The bulk modulus is a coefficient for the change in volume for a given uniform pressure. Expressed by terms of physics, the bulk modulus K is expressed as[21]

$$K = -V\frac{dP}{dV}, \tag{2.2}$$

which must be larger than zero, such that the change in volume is negative.

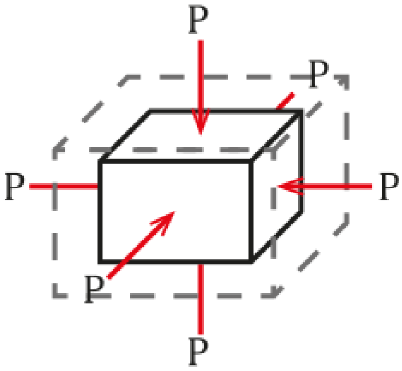

Figure 2.2: A uniform volume compression[22].

2.1.3 Poisson ratio

Poisson ratio is the ratio of transverse contraction strain to longitudinal extension strain in the direction of a stretching force. In terms of physics, the Poisson ratio is calculated as

$$\nu = -\frac{\varepsilon_{\text{trans}}}{\varepsilon_{\text{longitudinal}}}, \tag{2.3}$$

where the strain ε is defined as the change in a length ΔL divided by the original length L

$$\varepsilon = \frac{\Delta L}{L}. \tag{2.4}$$

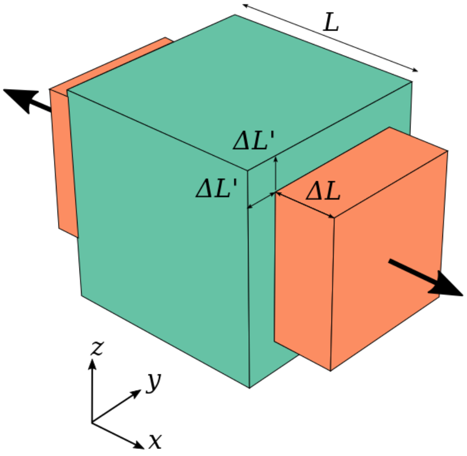

Figure 2.3: A cube with sides of length L of an isotropic linearly elastic material subjected to a tension along the x-axis. The green cube is unstrained, the red cube is expanded due to tension. Poisson ratio $\nu \approx 0.5$[23].

The Poisson ratio is directly related to the shear modulus and bulk modulus of a material through the relation

$$\nu = \frac{3K - 2G}{2(3K + G)}, \tag{2.5}$$

where K is the bulk modulus, and G is the shear modulus of the material[23].

2.2 Ultrasound physics

Ultrasound imaging is the process where a transmitted wave is reflected. The received signals are after that used to generate an image of the scattering medium. The wave equation gives the relation between the non-linear elasticity and the speed of sound of a medium. A particle has an equilibrium position $\vec{r}$ in space at a time t. The particle's displacement, change in position relative to its reference frame, is given by the Lagrangian $\Psi(\vec{r}, t)$. The nonlinear scattering builds on the relations described by the constitutive material equations given by

$$-\nabla \cdot \Psi(\vec{r},t) = \kappa(\vec{r})p(\vec{r}) - \beta_{\mathrm{n}}(\vec{r})(\kappa(\vec{r})p(\vec{r}))^2 + \kappa(\vec{r})h * p(\vec{r}), \tag{2.6}$$

where $\kappa(\vec{r})$ is the bulk compressibility at a position $\vec{r}$, the convolution kernel h describes the loss of energy after absorption, and $p(\vec{r})$ is the pressure at the particle's equilibrium position. β_{n} is the coefficient of non-linearity describing the medium's non-linearity

$$\beta_{\mathrm{n}} = 1 + \frac{B}{2A}, \tag{2.7}$$

consisting of the two parameters A and B, which are the first and second terms of the Taylor expansion of the pressure as a function of the density. The tissue of a human has non-linear properties. This results in the compressibility κ and the density ρ of the tissue will change nonlinearly with applied pressure. The constitutive material equation consists of the nonlinear elastic compressibility equation $K(\vec{r},p(\vec{r}))$, valid for very rapid compression of a material in soft tissue

$$\begin{aligned} K(\vec{r},p(\vec{r})) &= \kappa(\vec{r})p(\vec{r}) - \beta_{\mathrm{n}}(\vec{r})(\kappa(\vec{r})p(\vec{r}))^2 \\ &= \kappa(\vec{r})p(\vec{r})(1 - \beta_{\mathrm{n}}(\vec{r}))\kappa(\vec{r})p(\vec{r}) \\ &= \kappa(\vec{r})p(\vec{r}) + K_{\mathrm{n}}(\vec{r},p(\vec{r})), \end{aligned} \tag{2.8}$$

where

$$K_{\mathrm{n}}(\vec{r},p(\vec{r})) = -\beta_{\mathrm{n}}(\vec{r})(\kappa(\vec{r})p(\vec{r}))^2, \tag{2.9}$$

is the nonlinear part of the nonlinear elastic compressibility function $K(\vec{r})$ and $\kappa(\vec{r})$, consisting of β_{n}, the coefficient of non-linearity. For a heterogeneous material, the material parameters will get spatial variations. These varying fluctuations are usually separated in slow, subscript a and fast, subscript f, variations. The linear scattering originates from the linear variations in compressibility and mass density and have the linear scattering components $\gamma(\vec{r})$ and $\sigma_{\mathrm{l}}(\vec{r})$

$$\gamma(\vec{r}) = \frac{\rho_{\mathrm{f}}(\vec{r})}{\rho_{\mathrm{a}}(\vec{r}}, \tag{2.10}$$

$$\sigma_{\mathrm{l}}(\vec{r}) = \frac{\kappa_{\mathrm{f}}(\vec{r})}{\kappa_{\mathrm{a}}(\vec{r})}. \tag{2.11}$$

The nonlinear scattering component depends on the pressure at the position $\vec{r}$, describes the nonlinear elasticity in soft tissue

$$\begin{aligned} \sigma_{\mathrm{nl}}(\vec{r},p) = (2\beta_{\mathrm{na}}(\vec{r})(2 + \sigma_{\mathrm{l}}(\vec{r}))\sigma_{\mathrm{l}}(\vec{r}) + \beta_{\mathrm{nf}}(\vec{r})(1 + \sigma_{\mathrm{l}}(\vec{r}))^2)\kappa_{\mathrm{a}}(\vec{r})p(\vec{r}) \\ \approx 4\beta_{\mathrm{na}}(\vec{r})\sigma_{\mathrm{l}}(\vec{r})\kappa_{\mathrm{a}}(\vec{r})p(\vec{r}), \end{aligned} \tag{2.12}$$

where the notation a and f means slow and fast parameters, and the nonlinear scattering is proportional to the linear scattering component $\sigma_l(\vec{r})$[24].

The constitutive material equation 2.6 also describes the relative volume compression of tissue as

$$\frac{\partial V}{\Delta V} = -\nabla\Psi(\vec{r},t), \tag{2.13}$$

leading to the nonlinear wave equation for a heterogeneous medium modeling the relative volume compression of tissue to second order

$$\begin{aligned}
&\underbrace{\nabla^2 p(\vec{r},t) - \frac{1}{c_0^2(\vec{r})}\frac{\partial^2 p(\vec{r},t)}{\partial t^2}}_{\text{Linear propagation}} + \underbrace{\frac{\beta_n(\vec{r})\kappa_a(\vec{r})}{c_0^2(\vec{r})}\frac{\partial^2 p(\vec{r},t)^2}{\partial t^2}}_{\text{Nonlinear propagation}} - \underbrace{h * \frac{1}{c_0^2(\vec{r})}\frac{\partial^2 p(\vec{r},t)}{\partial t^2}}_{\text{Absorption}} \\
&\quad = \underbrace{\frac{\sigma_l(\vec{r})}{c_0^2(\vec{r})}\frac{\partial^2 p(\vec{r},t)}{\partial t^2} + \nabla(\gamma(\vec{r})\nabla p(\vec{r},t))}_{\text{Linear scattering source terms}} - \underbrace{\frac{\sigma_{nl}(\vec{r})}{c_0^2(\vec{r})}\frac{\partial^2 p(\vec{r},t)^2}{\partial t^2}}_{\text{Nonlinear scattering source term}},
\end{aligned} \tag{2.14}$$

including forward propagation and the scattering phenomena. $c_0(\vec{r})$ from equation 2.14 is defined as

$$c_0(\vec{r}) = \frac{1}{\sqrt{\rho_\mathrm{a}(\vec{r})\kappa_\mathrm{a}(\vec{r})}}, \tag{2.15}$$

and is the linear wave propagation velocity. A modification of $c_0(\vec{r})$ gives the non linear wave propagation velocity, including β_n,

$$\begin{aligned}
c(\vec{r}, p(\vec{r},t)) &= \frac{1}{\sqrt{(\rho_\mathrm{a}(\vec{r})\kappa_\mathrm{a}(\vec{r}))(1 - 2\beta_\mathrm{n}(\vec{r})\kappa_\mathrm{a}(\vec{r})p(\vec{r},t))}}, \\
&\approx c_0(\vec{r})(1 + \beta_\mathrm{n}(\vec{r})\kappa_\mathrm{a}(\vec{r})p(\vec{r},t)),
\end{aligned} \tag{2.16}$$

taking the sum of the linear propagation velocity and the modification including β_n, the slow compressibility κ_a and the pressure function $p(\vec{r},t)$[24].

2.3 SURF imaging

SURF imaging is a dual-band imaging method developed at the Norwegian University of Science and Technology at the Department of Circulation and Medical Imaging. SURF imaging is an example of a nonlinear imaging technique dependent on the nonlinear characteristics of the tissue. It is dual-band as both a high frequency pulse (HF) and low frequency pulse (LF) are transmitted through the aperture at the same time as seen in figure 2.4.

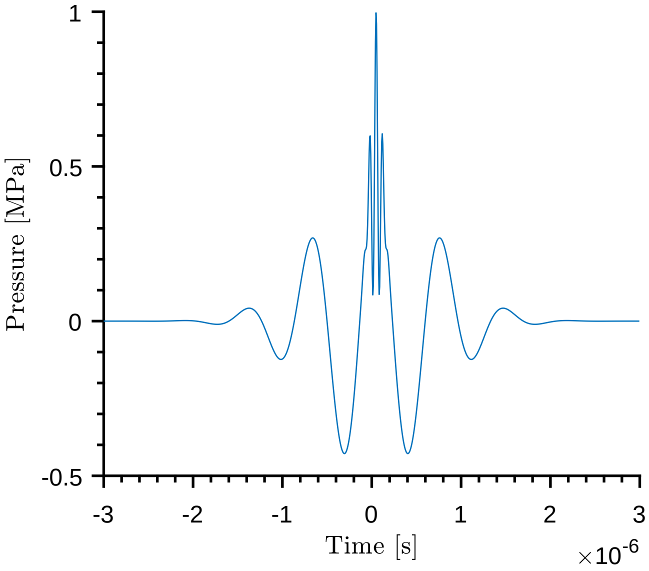

Figure 2.4: A HF pulse placed on a positive LF pulse.

In figure 2.4 a typical SURF pulse complex is visualised, the lower frequency LF pulse with a HF pulse of shorter period placed on the top. The LF pulse manipulates the nonlinear elasticity of the tissue, which makes the co-propagating HF pulse experiencing either an expansion or a compression of the tissue. This effect of a dual-band probe design has proved benefits in the detection of microbubbles and microcalcifications together with suppression of reverberations (multiple reflections) noise in ultrasound images[8]. The nonlinear manipulation by the LF pulse can be changed by using different LF polarities and amplitudes. A chosen reference value gives the amplitude of the LF pulse, p_{ref}, and a scaling factor of p giving the polarity and amplitude of LF, such as

$$p_{\text{LF}} = p \cdot p_{\text{ref}}. \tag{2.17}$$

The scaling factor p is usually given values in the range -2 to 2. Figure 2.5 shows an example of a SURF pulse complex where the LF pulse is of negative polarity. Transmitting multiple SURF pulses with different LF polarities and/or amplitudes may be sufficient in increasing non-linear scattering contrast to tissue-ratio (CTR)[8].

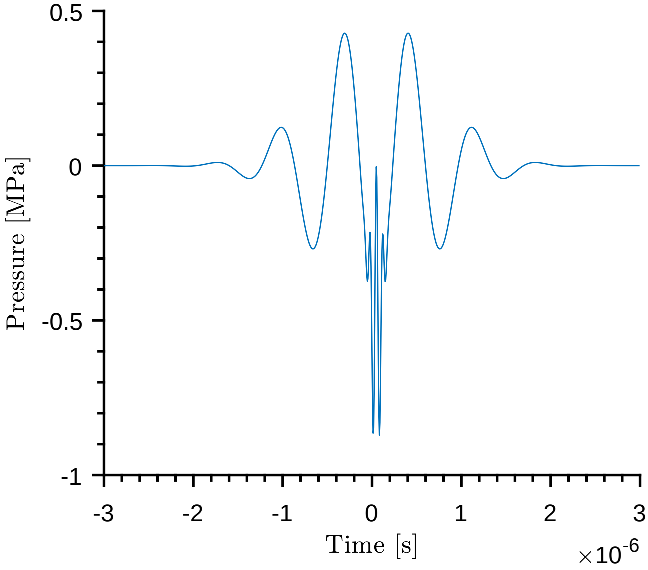

Figure 2.5: A HF pulse placed on a negative LF pulse.

In a SURF pulse, the modifying pressure p_{LF} varies over the HF pulse, which results in a LF-dependent distortion of the HF pulse. This is named Pulse Form Distortion (PFD), the HF pulse experiences an alteration of its original shape. The propagation time of the combined SURF pulse will due to PFD change, this is denoted by Non-linear Propagation Delay (NPD). The pressure of a SURF pulse complex is

$$p = p_{\mathrm{LF}} + p_{\mathrm{HF}}. \tag{2.18}$$

The nonlinear propagation and scattering are in 2nd order approximation both given by

$$p^2 = (p_{\mathrm{LF}} + p_{\mathrm{HF}})^2 = \underbrace{p_{\mathrm{LF}}^2}_{\text{Nonlinear self distortion}} + \underbrace{2p_{\mathrm{LF}}p_{\mathrm{HF}}}_{\text{Nonlinear interaction}} + \underbrace{p_{\mathrm{HF}}^2}_{\text{Nonlinear self distortion}} , \tag{2.19}$$

introducing the interaction between the HF and LF pulses by p_{LF} and p_{HF}. The modification by the LF pulse of the medium's elasticity is equivalent with modification of the propagation velocity. This is written as

$$c(r,t) = c_0(r,t)\sqrt{1 + 2\beta_{\mathrm{n}}(r)\kappa(r)p_{\mathrm{LF}}(r,t)}. \tag{2.20}$$

β_{n} is the coefficient of non-linearity, κ is the bulk compressibility of the medium, and p_{LF} is the pressure amplitude of the LF pulse. Equation 2.20 shows the modification of propagation velocity by transmitting a combined SURF pulse complex, compared to only transmitting a HF pulse. Altering the amplitude of the LF pulse by p_{LF} will change the propagation velocity and time of the SURF pulse, leading to either advancement or non-linear propagation delay.

2.3.1 Pulse Form Distortion

Different pressures in the LF pulse across the HF pulse causes a change in propagation velocity of the HF pulse. This creates a PFD of the HF pulse, and the increased overall pressure also increases the self-distortion of the HF pulse. The PFD of the HF pulse depends on the polarity and amplitude of p_{LF}, as well as the positioning of the HF pulse on the LF pulse.

The manipulation of a HF pulse when placed on top of a LF pulse is approximated as constant. However, when the HF pulse is placed on either the upwards or downwards raising gradient of the LF pulse, the manipulation is no longer considered uniform. The end and start of the HF pulse will no longer experience the same propagation velocity. For the downwards gradient, the HF pulse is compressed, as the end of the pulse experiences a faster propagation velocity. For the upwards raising gradient, an expansion results in the start of the HF pulse propagating faster than the end of the pulse. Diffraction of the LF pulse with depth also produces an oscillation of the HF gradient position, producing the HF position to slide with depth[25].

The PFD of a received HF pulse has not yet shown to follow a mathematical. Therefore, it is related to the comparison of a HF pulse transmitted separately, and HF pulse transmitted simultaneously with a co-propagating LF. With a large bandwidth of the HF pulse and high enough difference between the frequencies of HF and LF pulses, it is possible to modify the pulse form distortion by the LF pulse with a PFD filter. This is possible as the sum and difference spectra generated due to NPD overlap[25].

Equation 2.19 shows the nonlinear self-distortion of HF, which is also an effect of the nonlinear propagation up to the first scattering. For nonlinear propagation, the energy from the main frequency band is moved up into harmonic bands, resulting in self-distortion of the HF pulse.

2.4 Ultrasound radiation force

A force called Ultrasound Radiation Force (URF) acts on a medium when a transmitted ultrasound wave passes through it. The medium experiences a transferal of momentum from the wave. The resulting force, F, comes from both scattering and absorption[26]. The absorption-generated force is calculated as

$$F_{\mathrm{a}}(\vec{r},\omega) = \frac{1}{c}\sigma_{\mathrm{a}}(\vec{r},\omega)I_{\mathrm{a}}(\vec{r},\omega), \tag{2.21}$$

where c is the speed of sound, σ_{a} is called the medium's extinction coefficient from absorption and the temporal average intensity is denoted I_{a}. Experiments have shown σ_a to follow a power law in frequency, therefore the fraction of ω and ω_0 is taken the exponent of given by $b(r)$. Further, α_0 is the absorption coefficient of the medium, ω_0 is the reference value of the angular frequency, $b(r)$ describes the dependency on the frequency,

$$\sigma_{\mathrm{a}}(\vec{r},\omega) = \alpha_0(\vec{r})(\frac{\omega}{\omega_0})^{b(\vec{r})}. \tag{2.22}$$

Equations 2.21 and 2.22 give a direct relationship between the radiation force and frequency, as the extinction coefficient increases with frequency. The change of the temporal average intensity in depth, is calculated by σ_a and $I_a(\vec{r}, \omega)$ as

$$\frac{\mathrm{d}I(\vec{r}, \omega)}{\mathrm{d}z} = \sigma_a(\vec{r}, \omega) I_a(\vec{r}, \omega). \tag{2.23}$$

For objects embedded in the tissue, radiation force will also be generated due to scattering from the object. An equation for the total radiation force on the particle looks like

$$F(\vec{r}, \omega) = \frac{1}{c} \sigma_e(\vec{r}, \omega) I_a(\vec{r}, \omega), \tag{2.24}$$

$$\sigma_e(\vec{r}, \omega) = \sigma_a(\vec{r}, \omega) + \sigma_s(\vec{r}, \omega), \tag{2.25}$$

where both scattering and absorption are included in the extinction cross section per unit volume $\sigma_e(\vec{r}, \omega)$. The calculation of the extinction coefficient σ_a from absorption is shown in 2.22. The scattering from the particle is dependent on the frequency, which again is dependent on the radius of the scattering object relative to the wavelength λ of the ultrasound pulse. Therefore, to calculate the radiation force from scattering, it is necessary to derive formulas where the size of the scattering object is taken into consideration. This is presented in next section.

Another way of writing the radiation force is done in [27]. A pressure $p(\vec{r}, t)$ acting on a surface S of a volume V produces a net force $\vec{F}$ on the volume as in

$$\vec{F} = -\int_S d^2 r \vec{n} p(\vec{r}, t) = -\int_V d^3 r \nabla p(\vec{r}, t), \tag{2.26}$$

where the normal vector $\vec{n}$ is pointing outwards, and the force has a similar form as a pressure gradient acting on a volume. In calculations of the ultrasound radiation force in the stationary displacement simulations in this thesis, the formula in equation 2.24 is rewritten as

$$F = \frac{\sigma_\mathrm{e} |p|^2}{2 Z_0 c} = \frac{\alpha_\mathrm{e} f |10^3 \mathrm{MI} \sqrt{f}|^2}{2 \rho c^2}, \tag{2.27}$$

where $Z_0 = \rho c$ is the acoustic impedance of a medium. $p = 10^3 \mathrm{MI} \sqrt{f}$ is the incident pressure wave pulse amplitude determined from limitations of the mechanical index MI and the driving frequency f. For a constant MI, the radiation force increases with $\sim f^2$ [28].

2.4.1 Radiation force from scattering

Solving the acoustic radiation force by a spherical scatterer has been investigated for decades. In practice, the incident acoustic field has a form of a beam that cannot be considered as a plane or spherical wave. For high-frequency focused transducers, the incident field is not necessarily uniform on the scale of the size of the scatterer[29].

In one specific situation, for a scattering sphere with a diameter much smaller then the wavelength, it is possible to derive the radiation force analytically. When the sphere is so small, it is considered a microparticle, and it is possible to only consider the monopole and dipole terms of the diffracted fields. The radiation force can be expressed as, $F = -\nabla U$, where U is a potential function. Viscosity and interaction between microparticles are neglected, and of the relation particle radius a and the wavelength λ it is assumed

$$a \ll \lambda. \tag{2.28}$$

Further, the force from both the incoming wave and the scattered wave is based on scattering theory and Navier-Stokes equations derived as

$$F_{rad} = \frac{-4\pi}{3} a^3 \nabla [\frac{1}{2} Re[f_1] \kappa_0 \langle p_{in}^2 \rangle - \frac{3}{4} Re[f_2] \rho_0 \langle v_{in}^2 \rangle]. \tag{2.29}$$

Radiation force due to scattering is generated due to differences in the acoustic properties of the scattering particle and its surrounding medium. These material properties are included in equation 2.29. The coefficients f_1 and f_2 are named monopole and dipole coefficients, giving relations between the compressibilities and densities of the particle and the surrounding tissue

$$f_1 = 1 - \frac{\kappa_0}{\kappa_\mathrm{p}} \quad \text{and} \quad f_2 = \frac{2(\rho_\mathrm{p} - \rho_0)}{2\rho_\mathrm{p} + \rho_0}, \tag{2.30}$$

where κ_p and ρ_p are the compressibility and density of the particle. κ_0 and ρ_0 is the tissue's compressibility and density[30]. However, with the assumption as in 2.28, it is of desire to calculate the radiation force produced by arbitrary incident waves, regardless of the size of the scatterer. For an incident wave acting on a scatterer, radiation force appears as a result of both the incident and scattered waves. For a known acoustic field, the radiation force can be calculated. The scatterer is in the following calculations assumed to be in an ideal fluid, such that the effects of viscosity and thermal conductivity are neglected. A change in wave momentum due to scattering at a sphere results in radiation force. The general formula for all forces by momentum fluxes on a closed surface of integration S is

$$F = \int_S T \mathbf{n} d\mathbf{a}, \tag{2.31}$$

where S is any fixed surface enclosing the scatterer. Gor'Kov has used this fact obtaining a closed-form analytical expression for the force on a particle in an arbitrary acoustic field. Implementing such a method is done by solving the acoustic problem, and the result is used to compute the momentum flux of second order. [30] derives the second-order flux as

$$T = \frac{1}{2} \rho \langle v^2 \rangle - \frac{1}{2\rho c^2} \langle p_\mathrm{t}^2 \rangle, \tag{2.32}$$

which is only valid when viscous and thermal losses are neglected. p_t is the acoustic pressure and is the total pressure variation of the coherent field. The syntax $\langle\rangle$ means time-averaging. Only the first order of perturbation of the pressure field for linear approximation of acoustic propagation is considered. As the momentum flux-integral is over a surface S

depending on time, integration is transformed to an equilibrium surface S_0 to enclose the particle, as by Yosioka and Kawasima[31]

$$F_{rad} = \int_{S_0} T\mathbf{n}d\mathbf{a} - \int_{S_0} \rho\langle(\mathbf{vn})\cdot n\rangle)d\mathbf{a}. \tag{2.33}$$

This is valid for all particles as long as the stress T from equation 2.32 is given, where the error has been compensated for by the addition of a convective momentum flux term. The acoustic pressure and velocity in equation 2.32 is solved by the acoustics problem and substituted into the integral in 2.33[32].

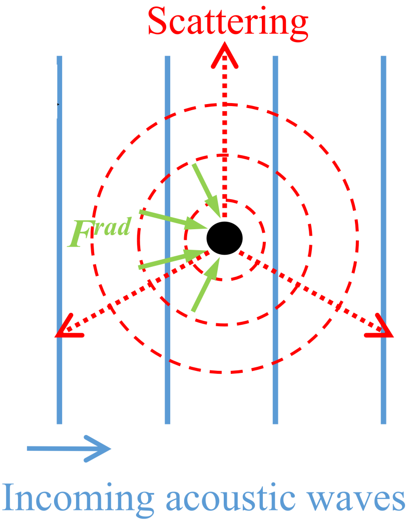

Figure 2.6: The generation of radiation force from scattering on a particle with acoustic waves coming in[33].

2.5 Displacement of a sphere in soft tissue

The theory in this section is adopted from a SURF technology in-house document [28], where Bjørn Angelsen has calculated different cases of sphere displacements in soft tissue analytically. The solutions are derived to be compared to numerical simulations of the displacement problem. This section first introduces the generation of pressure and shear waves in soft tissue. After that, low-frequency fields are calculated, solving for a stationary forced sphere embedded in tissue. The section ends by deriving a resonance frequency for a force applied as a function of time $F(t)$.

2.5.1 Shear waves in tissue

2.5.1.1 Fundamental equations for p and s waves

From [24] the acceleration equation in Cartesian coordinates is given by

$$\rho \frac{\partial^2 \psi_{\mathrm{i}}}{\partial t^2} = \frac{\partial T_{\mathrm{ij}}}{dx_{\mathrm{j}}} + f_{\mathrm{i}}, \tag{2.34}$$

where f is an acceleration force acting on the volume, for example a radiation force. The elasticity equation from [24] is

$$T_{\mathrm{ij}} = \lambda \varepsilon_{\mathrm{kk}} \delta_{\mathrm{ij}} + 2\mu \varepsilon_{\mathrm{ij}}, \tag{2.35}$$

where μ is the shear modulus, and the strain ε is

$$\varepsilon_{\mathrm{ij}} = \frac{1}{2}\left(\frac{\partial \psi_{\mathrm{i}}}{\partial x_{\mathrm{j}}} + \frac{\partial \psi_{\mathrm{j}}}{\partial x_{\mathrm{i}}}\right). \tag{2.36}$$

There is also the relation $\varepsilon_{\mathrm{kk}} = \varepsilon_{11} + \varepsilon_{22} + \varepsilon_{33} = \nabla \psi$. Inserting equation 2.36 and equation 2.35 into equation 2.34 gives

$$\rho \frac{\partial^2 \psi}{\partial t^2} = \mu \nabla^2 \vec{\psi} + (\lambda + \mu) \nabla (\nabla \vec{\psi}) + \vec{f}. \tag{2.37}$$

The Helmholtz vector decomposition is [34]

$$\begin{aligned} \vec{\psi} = -\nabla \varphi + \nabla \times \vec{\sigma} = \vec{\sigma}_{\mathrm{p}} + \vec{\psi}_{\mathrm{s}} \quad \vec{\psi}_{\mathrm{p}} = -\nabla \varphi \quad \nabla \times \vec{\psi}_{\mathrm{p}} = 0 \quad \vec{\psi}_{\mathrm{s}} = \nabla \times \vec{\sigma} \quad \nabla \vec{\psi}_{\mathrm{s}} = 0, \\ \vec{f} = -\nabla \vec{F} + \nabla \times \vec{G} = \vec{f}_{\mathrm{p}} + \vec{f}_{\mathrm{s}} \quad \vec{f}_{\mathrm{p}} = -\nabla \vec{F} \quad \nabla \times \vec{f}_{p} = 0 \quad \vec{f}_{\mathrm{s}} = \nabla \times \vec{G} \quad \nabla \vec{f}_{\mathrm{s}} = 0, \end{aligned} \tag{2.38}$$

which is utilized such that equation 2.37 can be rewritten as

$$-\rho \nabla \frac{\partial^2 \phi}{\partial t^2} + \rho \nabla \times \frac{\partial^2 \vec{\sigma}}{\partial t^2} = \nabla(-(\lambda + 2\mu) \nabla^2 \phi - F) + \nabla \times (\mu \nabla^2 \vec{\sigma} + \vec{G}). \tag{2.39}$$

It is of interest separating equation 2.39 into pressure- and shear-wave equations such as

$$p: \quad \rho \frac{\partial^2 \phi}{\partial t^2} - (\lambda + 2\mu) \nabla^2 \phi = F \qquad s: \quad \rho \frac{\partial^2 \vec{\sigma}}{\partial t^2} = \mu \nabla^2 \vec{\sigma} = \vec{G}. \tag{2.40}$$

Taking the gradient of the pressure-wave equation and curl of the shear-wave equation gives

$$\begin{aligned} \nabla^2 \vec{\psi}_{\mathrm{p}} - \frac{1}{c_{\mathrm{p}}^2} \frac{\partial^2 \vec{\psi}_{\mathrm{p}}}{\partial t^2} = -\frac{1}{\lambda + 2\mu} \vec{f}_{\mathrm{p}} \quad c_{\mathrm{p}} = \sqrt{\frac{\lambda + 2\mu}{\rho}} \quad \nabla \times \vec{\psi}_{\mathrm{p}} = \nabla \times \vec{f}_{\mathrm{p}} = 0, \\ \nabla^2 \vec{\psi}_{\mathrm{s}} - \frac{1}{c_{\mathrm{s}}^2} \frac{\partial^2 \vec{\psi}_{\mathrm{s}}}{\partial t^2} = -\frac{1}{\mu} \vec{f}_{\mathrm{s}} \quad c_{\mathrm{s}} = \sqrt{\frac{\mu}{\rho}} \quad \nabla \vec{\psi}_{\mathrm{s}} = \nabla \vec{f}_{\mathrm{s}} = 0. \end{aligned} \tag{2.41}$$

A general force for pressure- and shear-waves is

$$\begin{aligned} \vec{f}_{\mathrm{p}}(\vec{R}) &= -\frac{1}{4\pi} \int d^3 R_1 \nabla \left(\vec{f}(\vec{R}_1) \frac{1}{|\vec{R} - \vec{R}_1|}\right) \\ \vec{f}_{\mathrm{s}}(\vec{R}) &= \vec{f}(\vec{R}) + \frac{1}{4\pi} \int d^3 R_1 \nabla \left(\vec{f}(\vec{R}_1) \nabla \frac{1}{|\vec{R} - \vec{R}_1|}\right) \end{aligned} \tag{2.42}$$

2.5.1.2 Point source shear waves

A point source simplifies the analytic evaluation of the solution

$$\vec{f}(\vec{R})h(t) = \delta(\vec{R})h(t)\vec{e}_3. \tag{2.43}$$

For shear waves the point source is a strong assumption due to the low propagation velocity $c_s \approx$ 1 m/s to 10 m/s in soft tissue. The shear-wave propagates across a microcalcification of radius 200 µm in a time of $\approx$ 200 µs to 20 µs. For a period t of 10 µs for the ultrasound pulse $h(t)$, the wave front propagates only a distance $R_\mathrm{p} \approx$ 10 µm to 100 µm, which is short due to the dimension R_s of typical forces $\vec{f}(\vec{R})$. For $R_\mathrm{s} =$ 1 mm and $c_\mathrm{s} =$ 2 mm/ms the total period of shear displacement is $T_\mathrm{s} = R_\mathrm{s}/c_\mathrm{s} =$ 500 µs. Hence, even small sources appears as and extended source with different source points so that the duration of the shear wave pulse is longer than the calculated shear displacement T_s of $h(t)$.

The pulse bandwidth $f_\mathrm{max} \approx 1/2T_\mathrm{p} \approx$ 50 kHz. With a shear-wave speed $c_\mathrm{s} \approx$ 1 m/s to 10 m/s representing a minimal λ wavelength of 20 µm to 200 µm, the analytic expressions from a point source gives indications of the shear wave from sources of practical dimensions.

For the pressure-wave the propagation velocity in a soft tissue is $c_\mathrm{p} \approx$ 1500 m/s = 1.5 mm/µs. The pressure-wave hence moves across a micro calcification in a time of 0.13 µs, indicating that a vibrating microcalcification appears as a point source. By several calculations, the shear wave far-field is calculated from the shear wave equation in equation 2.41 as

$$\vec{\Psi}_\mathrm{s}(\vec{R}, t) = \frac{h(t - R/c_\mathrm{s})}{4\pi\mu R} cos(\theta)\vec{e}_\theta. \tag{2.44}$$

When the source has a spatial extension, the solution is a sum of such point source solutions with different source points. Due to the low propagation of shear waves in soft tissue, an extension in shear wave pulse length is produced, which often is considerable.

2.5.1.3 Point source pressure waves

In soft tissue, the pressure wave velocity c_p is usually much higher than the shear wave velocity c_s. The requirement of point source approximation is therefore not as strong as for the shear wave point source. Approximating $\lambda + 2\mu \approx \lambda$ makes the far-field approximation for the volume compression field from a dipole source to be written as

$$\vec{\Psi}_\mathrm{p}(R, \theta, t) = \frac{h(t - R/c_\mathrm{p})}{4\pi\lambda R} sin(\theta)\vec{e}_\mathrm{R}, \tag{2.45}$$

where it is noticed that Ψ_p and Ψ_s in equations 2.44 and 2.45 have differences in the numerator by λ and μ. In soft tissue under normal conditions, $\lambda >> \mu$, such that the total wave displacement is dominated by the shear displacement, even though the pressure and shear stresses are of the same magnitude.

2.5.2 Low frequency fields

2.5.2.1 Basic equations

For further investigations it is of interest to study the specific situation where the induced displacements are of the approximation $|\vec{R} - \vec{R}_0| << \lambda$. This gives

$$k|\vec{R} - \vec{R}_0| = \frac{2\pi}{\lambda}|\vec{R} - \vec{R}_0| \approx 0 \Leftrightarrow h(t - |\vec{R} - \vec{R}_0|/c) \approx h(t). \tag{2.46}$$

For soft tissue it is approximated $\mu \sim 10^{-5}\lambda$, and a situation where the total wave displacement is dominated by the shear wave displacement. The total displacement field is

$$\vec{\Psi}(\vec{R}, t) = \frac{h(t)}{4\pi\mu} \int d^3R_0 \frac{1}{|\vec{R} - \vec{R}_0|}(\vec{f}(\vec{R}_0) + \int d^3R_1 \nabla_0(\vec{f}(\vec{R}_1)\nabla_0 \frac{1}{|\vec{R} - \vec{R}_0|})), \tag{2.47}$$

where the total displacement comprises both a volume compression and a shear deformation term. The last term in equation 2.47 is dominated by shear deformation so that the total displacement is mainly of the shear type where volume compression can be neglected.

2.5.2.2 Stationary forced displacement of microcalcification particle in soft tissue

Equation 2.47 is in the following subsection derived for a microcalcification particle approximated as a sphere embedded in soft tissue. An ultrasound pulse induces radiation force on the tissue. The microcalcification is approximated as a sphere of radius a, and the displacement is in the z-direction, $\vec{\Psi} = \Psi_{\vec{e}_3}$ after a force induced in the same direction, $\vec{F} = F_{\vec{e}_3}$. This problem is a similar problem of the force on a sphere in a viscous fluid with a Reynolds number of very low value, such that the convective acceleration can be neglected. The force is only applied to the sphere. With $\vec{u}(\vec{R})$ as the fluid velocity and $p(\vec{R})$ as the pressure applied, the stationary flow is

$$\nabla^2\vec{u}(\vec{R}) = \frac{1}{\mu}\nabla p(\vec{R}) \quad \nabla\vec{u}(\vec{R}) = 0 \Rightarrow \nabla^2 p(\vec{R}) = 0 \quad \vec{u}(a, \theta) = U\vec{e}_3. \tag{2.48}$$

A solution of the Stokes problem is given in [35]. Figures 2.7 and 2.8 show the shear stress and pressure on a sphere in stationary flow separately.

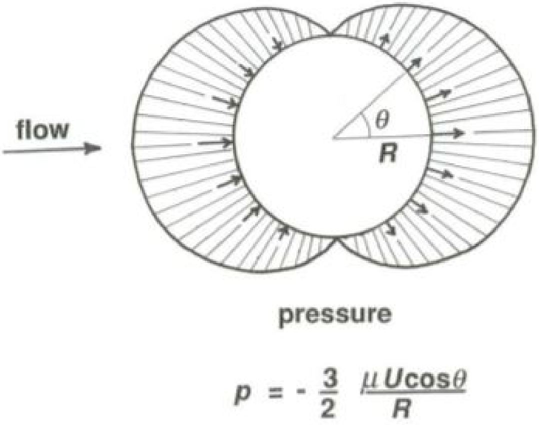
flow
θ
R
pressure
$p = -\frac{3}{2}\frac{\mu U \cos\theta}{R}$

Figure 2.7: The distribution of pressure-flow on a sphere surface in a flow of viscous fluid[35].

Figure 2.7 illustrates the distribution of pressure on the surface of a sphere in a flow of viscous fluid at very low Reynolds number. The distribution is shown in a planar section parallel to the flow direction and passing through the center of the sphere[35].

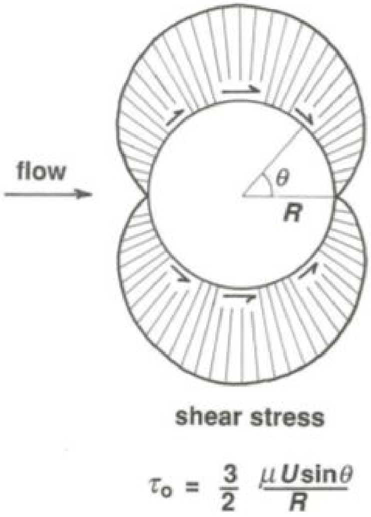
flow
θ
R
shear stress
$\tau_o = \frac{3}{2}\frac{\mu U \sin\theta}{R}$

Figure 2.8: The distribution of shear stress-flow on a spherical surface in a flow of viscous fluid[35].

Figure 2.8 illustrates the distribution of shear stress on the surface of a sphere in a flow of viscous fluid at very low Reynolds numbers. The distribution is shown in a planar section parallel to the flow direction and passing through the centre of the sphere[35]. The solution for the total force is the same as for the Stokes drag force. The total net Stokes force on a sphere is

$$F_{\mathrm{net}} = F_{\mathrm{drag}} = F_{\sigma} + F_{\mathrm{p}} = 4\pi a\mu\psi + 2\pi a\mu\psi = 6\pi a\mu\psi, \tag{2.49}$$

as it in the tissue volume can be shown to be zero volume force. F_{σ} is the contribution from shear stress on the sphere surface, F_{p} is the contribution from pressure on the sphere surface. The force from the shear stresses contributes twice than from the pressure. However, in equations 2.44 and 2.45 the total wave displacement is dominated by the shear displacement.

2.5.3 Low frequency pulsatile URF

The force F is typically a function of time, $F(t)$, such that the dynamic equation can be applied from Newtons 2nd law,

$$m\frac{d^2\Psi}{dt^2} + F_{\mathrm{drag}}\Psi = F. \tag{2.50}$$

Here the drag force F_{drag} and the experienced mass m by the sphere is found as

$$F_{\mathrm{drag}} = 6\pi\mu a \quad m = V_{\mathrm{p}}(\rho_{\mathrm{p}} - \rho_{\mathrm{t}}) = \frac{4}{3}\pi a^3(\rho_{\mathrm{p}} - \rho_{\mathrm{t}}), \tag{2.51}$$

where ρ_{p} is the density of the particle, ρ_{t} is the tissue density and a is the particle radius. The shear modulus μ is derived from the tissue density ρ_{t} and the shear wave velocity c_{s} in the tissue

$$\mu = \rho_{\mathrm{t}} c_{\mathrm{s}}^2. \tag{2.52}$$

Taking the pulse amplitude Fourier transform of equation 2.50 gives

$$-\omega^2\Psi m + F_{\mathrm{drag}}\Psi = F(\omega), \tag{2.53}$$

solving for Ψ,

$$\Psi = -\frac{1}{\omega^2 - \omega_{\mathrm{r}}^2}\frac{F(\omega)}{m}. \tag{2.54}$$

The resonance frequency is derived solving for ω_{r} as

$$f_{\mathrm{r}} = \frac{1}{2\pi}\omega_{\mathrm{r}} = \frac{1}{2\pi}\sqrt{\frac{9\rho_{\mathrm{t}}}{2(\rho_{\mathrm{p}} - \rho_{\mathrm{t}})}}\frac{c_{\mathrm{s}}}{a}. \tag{2.55}$$

In calculations the resonance frequency $f_{\mathrm{r}} \approx 1/a$. The resonance frequency is so close to a typical PRF of an ultrasound scanner, such that the microcalcification particle may excite resonance-like vibrations. Pulsed transmission may induce a radiation force that oscillates with the PRF. In these expressions and the further modelling in this thesis, the viscous component of the shear visco-elasticity of tissue is not included. In reality, the displacement-amplitude will be limited by this.

2.6 Nonlinear elastic quantification

In 2016, a new method introducing a nonlinear shear modulus of breast tissue was presented. The technique relies on acoustoelasticity theory in quasi-incompressible media. Under compression, static elastography and supersonic shear imaging are combined to register strain maps and shear modulus maps. The nonlinear shear modulus theory is based on the effect of uniaxial or hydrostatic pressure on the shear wave speed. For an isotropic and homogeneous material, where the axis of the uniaxial compression is parallel to the shear wave polarisation, and the shear wave displacement is smaller than static compression, by applying the Hooke's law, the nonlinear elastodynamic equation can be rewritten as

$$\rho V_{\mathrm{S}}^2 = \mu_0 - \sigma_{\mathrm{z}}\left(\frac{\mu_{\mathrm{nl}}}{12\mu_0}\right). \tag{2.56}$$

μ_0 is the materials shear modulus at a stress-free condition, μ_{nl} is the nonlinear shear modulus, σ_{z} is the stress applied in the z-direction and V_{S} is the shear wave velocity. Therefore, by measuring the shear wave speed as a function of stress applied, the nonlinear shear modulus μ_{nl} can be found[36]. Figure 2.9 suggests how the nonlinear shear modulus μ_{nl} can be measured on a breast phantom.

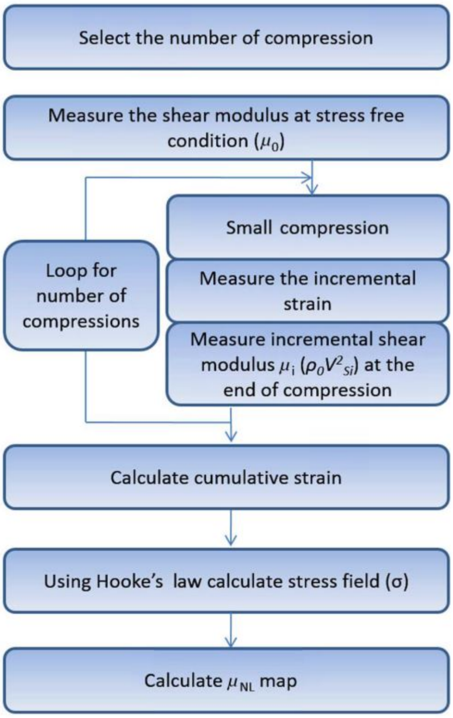
Select the number of compression
Measure the shear modulus at stress free condition (μ_0)
Small compression
Loop for number of compressions
Measure the incremental strain
Measure incremental shear modulus μ_i ($\rho_0 V^2_{si}$) at the end of compression
Calculate cumulative strain
Using Hooke's law calculate stress field (σ)
Calculate μ_{NL} map

Figure 2.9: The calculation of the nonlinear shear modulus[19].

2.7 Bubble physics

A microbubble may be in a crevice or on the surface of a microcalcification. Microbubbles are gas-filled spheres with radius $R_0 \approx 1\,\mu\text{m}$ to $10\,\mu\text{m}$. Theory for the behaviour of a microbubble in a crevice does not yet exist, as the shape can then not be considered spherical. In fluid mechanics, the Rayleigh-Plesset equation describes the dynamics of a spherical bubble in an infinite body of incompressible fluid. Its general form is written as an ordinary differential equation as

$$R\frac{d^2R}{dt^2} + \frac{3}{2}(\frac{dR}{dt^2})^2 + \frac{4\nu_{\mathrm{L}}}{R}\frac{dR}{dt} + \frac{2\gamma}{\rho_{\mathrm{L}}R} + \frac{\Delta P(t)}{\rho_{\mathrm{L}}} = 0, \tag{2.57}$$

where ρ_{L} is the density of the surrounding liquid, R is the radius of the bubble, ν_{L} is the kinematic viscosity of surrounding liquid and γ is the surface tension of the bubble-liquid interface. $\Delta P(t)$ is the difference between the externally pressure infinitely far from the bubble and the pressure within the bubble[37]. The free-space oscillation frequency of a microbubble without shell resonant and with equilibrium radius R_0, p_{g0} as equilibrium pressure, γ is the polytropic gas constant is presented as

$$f_{\mathrm{m}} = \frac{1}{2\pi R_0}\sqrt{\frac{3\gamma p_{\mathrm{g0}}}{\rho}}. \tag{2.58}$$

In free-space, the bubble oscillates as a spring pendulum. For a bubble close to a rigid boundary, the oscillating bubble will transfer momentum to surrounding fluid, experienced as micro-streaming. The surrounding fluid exerts shear stress on a rigid boundary, while the bubble exerts normal stress on the boundary. The largest stress will be at resonance frequency f_{m}. The maximum shear stress is calculated as

$$S_{\mathrm{m}} = \frac{2\sqrt{\nu\rho(\pi f_{\mathrm{m}})^3}(R_{\mathrm{max}} - R_0)^2}{R_0^2}, \tag{2.59}$$

where ν is the fluid viscosity, ρ is the fluid density and f is the driving frequency[38].

Chapter 3

Measurement setup

The measurement setup used for experiments done in this project is presented in this chapter. B-flow imaging experiments are performed on a GE Vivid E9-2 scanner. The experiment is supposed to visualise the generated flow induced by the HF pulse in a SURF pulse. The setup on the SURF scanner is used to provide dual-band ultrasound images of microcalcifications. The experiments are performed on a multi-modality breast-mimicking phantom with embedded microcalcifications.

3.1 GE Vivid E9-2

A GE Vivid E9-2 scanner was loaned by ISB to perform experiments on the B-flow Twinkling Sign Artifact, as the SURF scanner does not have Color Flow or B-flow imaging modes. With the success and expansion of 4D cardiac imaging, GE Vivid E9-2 was completely redesigned from the GE Vivid 7 Dimension with an emphasis on 4D cardiac imaging and solid ergonomics. GE Vivid E9 is a highly customizable powerful shared-service system considered to be the most versatile and top performing cardiac ultrasound machine, featuring eight times the processing power compared to conventional ultrasound machines. The machine allows a wide range of transducers as well as features. B-mode, M-mode, PW/CW/COLOR/Power Doppler and B-Flow and Blood Flow imaging are just some of $\sim$ 40 modes available[39].

3.1.1 B-flow imaging

B-flow is a technique developed by GE Medical Systems that extends the resolution, frame rate, and dynamic range of normal B-mode imaging to simultaneously image both blood flow and tissue. B-flow relies on coded excitation to boost weak signals from blood scatterers and on tissue equalization to simultaneously display flowing blood and tissue without threshold decision and overlay[10].

3.1.2 9L linear probe

A 9L linear probe was chosen to represent HF pulse imaging. Its applications are imaging of small parts, vascular, abdomen and pediatrics. The frequency range of the probe is 3.1 MHz to 10 MHz[40]. The probe application chosen was Carotid, the center frequency for this mode is either 8 MHz or 4 MHz, in this thesis a center frequency of 8 MHz was used. The pulse repetition frequency used was 5 kHz and the focus depth was 40 mm. The 9L linear probe is a commercial product, such that more detailed specifications are not possible to find for presentation.

3.2 The SURF scanner

The SURF scanner produces both a LF pulse and a HF pulse simultaneously. An Ultrasonix SonixMDP scanner transmits and receives the HF signals, and the LF pulses are transmitted by an Aurotech Manus. The hardware is controlled by the software on the SonixMDP. The signals received are signal processed in real-time on the scanner.

3.2.1 Vora-II dual-band imaging probe

Vora-II is a linear array transducer with two layers of piezoelectric materials and is the probe used on the SURF scanner. An acoustically isolating layer is between the two piezoelectric layers stacked upon each other. The first layer is connected to the Ultrasonix SonixMDP, generating HF pulses with a center frequency of 8 MHz, the second piezoelectric layer is connected to the Aurotech Manus generating LF pulses with a center frequency of 0.8 MHz. The mechanical setup in Vora-II makes it possible transmitting HF and LF pulses simultaneously through the same probe[9]. Transmit parameters for the probe are found in table 3.1.

Table 3.1: General transmit parameters of the Vora II probe

Parameter	HF	LF	Unit
Geometry	Linear	Linear	-
Center frequency	8	0.8	MHz
Number of periods	2	2.5	cycles
Element size (Azimuth)	300	900	µm
Element size (Elevation)	4	8	mm
Active elements (Azimuth)	128	58	-
Active elements (Elevation)	1	1	-
Focus depth (Azimuth)	20	∞	mm
Focus depth (Elevation)	14	14	mm
Apodization	No	No	-
Pulse polarities	$+/0/-$	$+/0/-$	-
Amplitude	10 V	15 V to 80 V	-

3.3 Multi-modality breast phantom

Experiments have been performed on a multi-modality breast phantom produced by Computerized Imaging Reference Systems, Inc (CIRS). The breast phantom, CIRS Model 073, accurately mimics the heterogeneous appearance of breast tissue under ultrasound, and has cystic and dense lesions embedded. Half of the dense lesions are spherical and have a 100 µm to 300 µm microcalcification embedded. The tissue mimicking material is self-healing and it re-seals if biopsy needle is used[41].

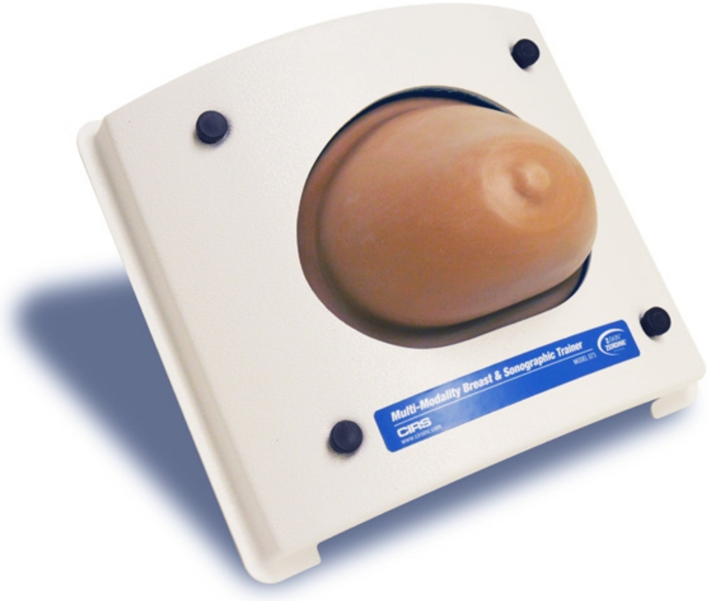

Figure 3.1: The Multi-Modality phantom CIRS Model 073 which is used in experiments[42].

Chapter 4

Simulation setup

This chapter presents the simulation tools used in this thesis and the study setups within them. For the generation of SURF pulses, as well as the calculation of the induced radiation force, the in-house simulation-software Wavesim is utilised. For simulations of the shear displacement of a microcalcification in breast tissue, COMSOL, a solver and multiphysics simulation software has been used. COMSOL solves physics problems numerically where the math is governed by Partial Differential Equations (PDEs). It exists similar tools as COMSOL, like ANSYS and ABAQUS. However, COMSOL was chosen as it can be integrated with Matlab, at the same time as the different modules available in COMSOL are well documented. The first section will describe the simulation setup in Wavesim, together with the chosen simulation parameters. Plots of generated pulses are shown beside the force fields calculated. The next section will approach how the displacement of a microcalcification in breast tissue is FEM-modelled in COMSOL. How and why the different modules are chosen will be reasoned. Some of the material presented in the first section on Wavesim is the same as in the project thesis[18].

4.1 Wavesim

Simulation of SURF pulses and calculation of the radiation force induced by the pulses are done using the simulation tool Wavesim. Johannes Kvam first developed the software in his master thesis in 2012[43], Wavesim has been further developed by the company since. The program generates and simulates the forward nonlinear propagation of SURF pulse complexes. For the research in this thesis, only the forward propagation has been simulated. Wavesim is beside implemented with simulation modes for backwards propagating after reflection, a mode for simulating reverberations, as well as other modes.

The front end of Wavesim is programmed in Matlab, providing an interface easy to use when performing simulations. The back end is programmed in C, where the parallel computing library OpenMP is used. OpenMP is a way to speed up serial code by parallelism, and multiple CPU cores are employed simultaneously running a program.

In the simulations, ultrasound pulses are transmitted using a transmit aperture which can be modified by the user. For the simulations of the radiation force from absorption, typical parameters for transmitting a SURF pulse are chosen, presented in table 4.1. The pulses are generated from parameters where the centre frequency, number of periods and amplitude are defined. Both polarities of a LF pulse and a HF pulse are simulated separately, as well as both a positive and negative SURF pulse complex. In Wavesim several material types can be chosen. The pulses are transmitted into the material. From the choice 'Muscle' to model a breast tissue in this thesis, Wavesim generates the medium as in table 4.2, specifying the speed of sound, absorption, compressibility, non-linearity coefficient and depth of the medium.

Table 4.1: Parameters of transmit aperture in Wavesim

Parameter	HF	LF	Unit
Geometry	Linear	Linear	-
Center frequency	8	0.8	MHz
Number of periods	2	2.5	cycles
Amplitude	0.5	0.5	MPa
Element size (Azimuth)	300	900	µm
Element size (Elevation)	4	8	mm
Active elements (Azimuth)	24	18	-
Active elements (Elevation)	1	1	-
Focus depth (Azimuth)	22	∞	mm
Focus depth (Elevation)	14	14	mm
Apodization	No	No	-
Offset	0	0	°

Table 4.2: Parameters of the chosen medium "Muscle" in pulse simulations

Parameter	Value	Unit
Speed of sound (c_0)	1549	m/s
Absorption coefficient (α)	0.52	dB/cmMHz
Compressibility (κ)	$3.927 \cdot 10^{-10}$	ms^2/kg
Coefficient of non-linearity (β_{n})	$3.9 \cdot 10^{6}$	-
Total depth of medium (z)	40	mm

For each simulation, the radiation force will be calculated for 5 pulses. Wavesim gives the opportunity to visualize the generated pulse profiles, to make sure the pulses are generated as purposed. The azimuth and elevation profiles are also included in the visualizations, the azimuth profile on top, the elevation profile thereafter. The positive SURF pulse complex from initial input parameters in table 4.1 is visualized in figure 4.1.

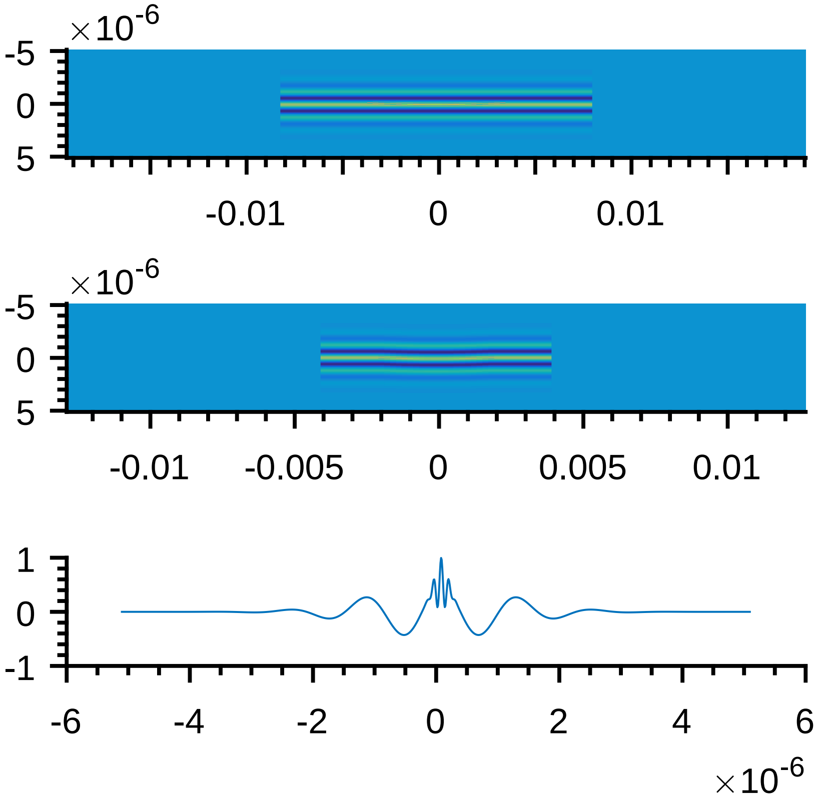

Figure 4.1: Azimuth profile, elevation profile and onaxis pulse profile for a positive SURF pulse generated in Wavesim.

The HF pulse with a short period is placed on top of the LF pulse, where the LF pulse has a longer period. Figure 4.2 shows how the HF pulse can be placed in other offsets than 0°, respectively −90° and 90° offsets are presented. The project thesis investigated how different offsets changed the amplitude of the radiation force induced[18]. However, the effect was minimal. Therefore the offset in the SURF pulses generated in this research is the initial offset of 0°.

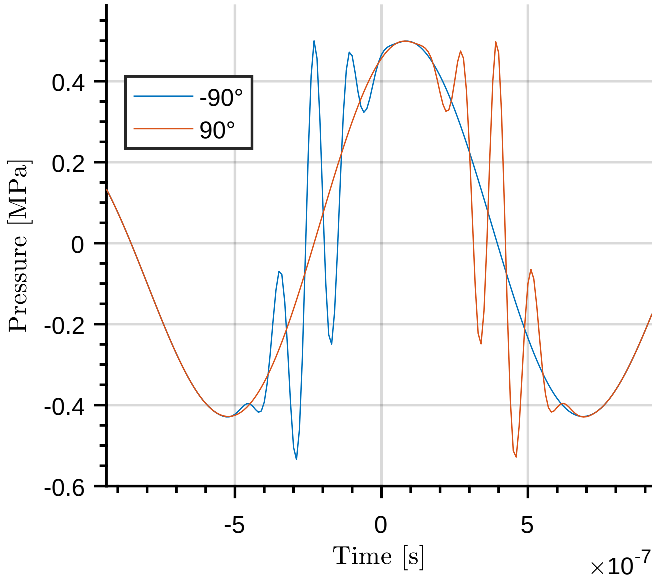

Figure 4.2: A HF pulse placed on a positive LF pulse with −90° and 90° offsets

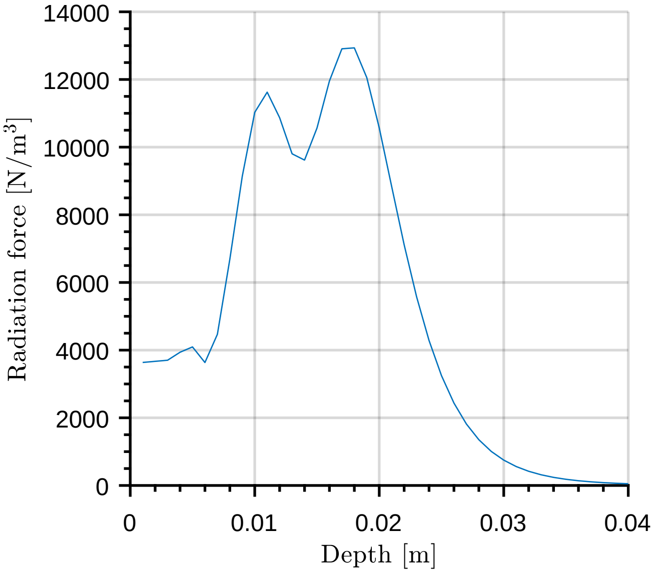

Figure 4.3: The onaxis radiation force induced by a SURF pulse.

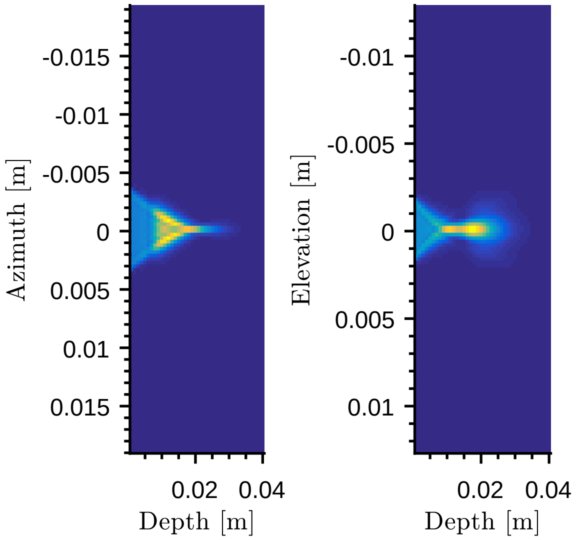

Figure 4.4: Azimuth and elevation radiation force profiles for a SURF pulse

After the pulses are generated, the radiation force is calculated per depth in the selected medium. This is done in Wavesim by equation 2.21. As equation 2.21 calculates the radiation force from absorption, the material parameters used in calculations are for the tissue as in table 4.2. Absorption occurs due to the surrounding tissue, not a microcalcification embedded within it. The radiation force is a force per unit volume, with [N/m^3] as the unit. For the force of absorption experienced by a specific microcalcification in [N] unit, the radiation force is multiplied by the volume of the microcalcification.

Figure 4.3 shows the onaxis radiation force generated by a SURF pulse. The depths of the two peaks are given by the elevation and azimuth focus in table 4.1. Figure 4.4 shows the azimuth and elevation radiation force profiles for a SURF pulse. The pulse is not apodized, such that the azimuth force profile has edge waves in $\sim$ 11 mm depth. The on-axis radiation force from a LF pulse is shown in figure 4.5. Figure 4.6 shows the azimuth and elevation force profiles for a LF pulse. Compared to the profiles for a SURF pulse in figure 4.4 these profiles are much wider. The contribution from the HF pulse dominates the radiation force induced by a SURF pulse complex.

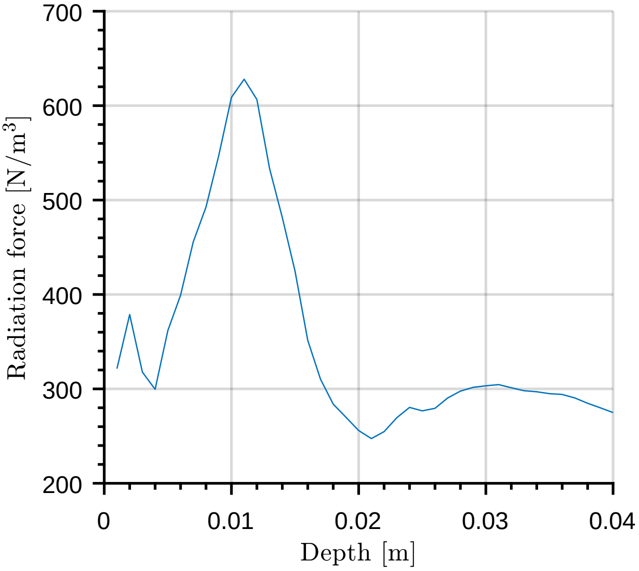

Figure 4.5: The onaxis radiation force induced by a LF pulse.

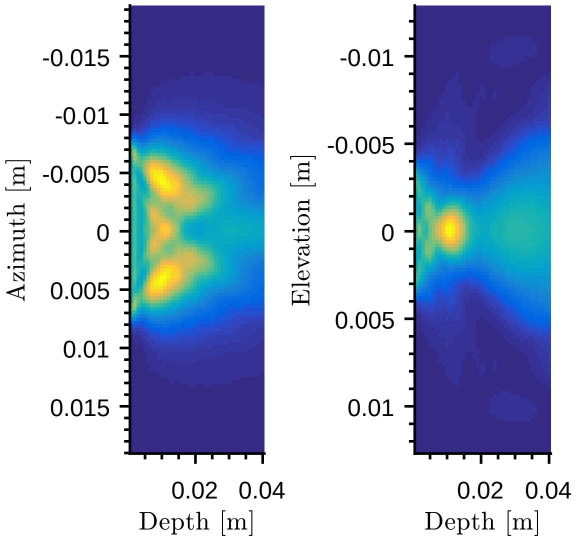

Figure 4.6: Azimuth and elevation radiation force profiles for a LF pulse.

4.2 COMSOL

COMSOL Multiphysics is a software solving multiphysics problems by a numerical approach. The program solves the displacement simulations of a microcalcification embedded in breast tissue performed in this project. COMSOL has been an effective tool as the numerical simulations have been performed at the same time as an analytic approach to the displacement problem. Exploiting two different approaches has lead to similar reasoning and mutual understanding.

COMSOL was by several reasons considered as the best tool. Firstly, it can be easily integrated with Matlab. As the force fields are generated in Wavesim in Matlab, this gives the opportunity to use realistic radiation force induced by a SURF pulse in COMSOL. Also, the program can be used without in-depth knowledge of physics or numerical analysis, as it includes predefined interfaces and modules for various engineering applications.

COMSOL gives the opportunity to choose between several physical interfaces, as well as coupling the interfaces between each other. In this thesis, only the Solid Mechanics module is used. Some specific material parameters are needed as input in Solid Mechanics, and COMSOL uses them in the further calculation of material properties such as shear and pressure wave velocities.

COMSOL generates a solution to the physics problem numerically by generating solution matrices, describing the behaviour of each element in the different domains. The meshing size describes the element sizes. The meshing size is important in the preciseness of the solution. The finer mesh, the more precise solution is generated numerically by COMSOL. However, finer mesh implies larger solution matrices, increasing the workload of a simulation. The next subsections describe the procedure in implementing the displacement simulations of a breast tissue in COMSOL.

4.2.1 Solid mechanics

The Solid mechanics interface is intended for a general structural analysis of 2D, 3D or axisymmetric bodies. In the model of a microcalcification embedded in breast tissue, an axisymmetric 2D body is modelled. The interface in Solid Mechanics is based on solving the equations of motion, together with a constitutive model for a solid material assigned with material properties. From these equations and properties, displacements, stresses and strains are computed by COMSOL. The displacement field $\mathbf{u}$ consists of u, w, which are the radial and vertical displacements. The displacement field $\mathbf{u}$ is denoted by the dependent variables of the solid mechanics interface[44].

4.2.2 Equation of motion

The first Piola-Kirchoff stress P is calculated from the second Piola-Kirchoff stress as $P = FS$. The first Piola-Kirchoff stress relates forces in the present configuration with areas in the reference configuration. By the first Piola-Kirchoff stress tensor, the equation of motion is written as

$$\rho_0 \frac{\partial^2 \mathbf{u}}{\partial t^2} = \mathbf{F}_\mathrm{V} - \nabla_\mathrm{X} \cdot P, \tag{4.1}$$

where the density ρ_0 is the material density in the initial undeformed state, $\mathbf{F}_\mathrm{V}$ is the volume force vector[44].

4.2.3 Linear elastic material

In modelling the elasticity in breast tissue, the Linear Elastic Material node was assigned to the domains of the microcalcification and surrounding tissue. In the Linear Elastic Material node, the isotropic linear elasticity is utilised. Isotropic linear elasticity was assigned as the materials are simplified to have uniform sensitivities in all directions. Only three independent material parameters are required in such a model. In the modelling done in this research, the density, shear modulus and bulk modulus were chosen as the three independent material parameters. These three material parameters were found most accurate for a microcalcification in [45]. For the breast tissue, the material parameters are the same as in [14]. The material parameters used in COMSOL are found in table 4.3. For a linear elastic material in COMSOL, the stress tensor is related to the elastic strain tensor of material by Hooke's law

$$\sigma = C : \varepsilon_\mathrm{el}, \tag{4.2}$$

where the parameter C is the 4th order elasticity tensor, the notation : means double dot tensor product. The elastic strain ε_el is the difference between the total strain and all inelastic strains[44].

Table 4.3: Domain parameters in COMSOL

Parameter	Muscle	Microcalcification	Unit
Shear modulus	3.6	$32 \cdot 10^3$	kPa
Bulk modulus	2.4	129.6	GPa
Density	1090	2711	kg/m^3

4.2.3.1 Nearly incompressible material

The nearly incompressible material is marked for the linear elastic material node assigned to the breast tissue. The Poisson ratio ν determines how much a material will possibly compress under uniaxial stress. By the material properties shear modulus and bulk modulus, the Poisson ratio is calculated in COMSOL by the formula in equation 2.5. When $\nu \approx 0.5$ the material is denoted incompressible. A fully incompressible material is very different from a compressible material, as there is no volume change. As a result, it is impossible to find a mean stress value from it. As the mean stress equation is

$$p = f(\nabla V), \tag{4.3}$$

$p = 0$ for an incompressible material. To avoid a phenomenon named locking, which occurs in COMSOL when Poisson ratio $\nu \approx 0.5$, the nearly incompressible material property is advised to be assigned under the linear elastic material properties[46]. For the material properties of breast tissue in 4.3 the Poisson ratio is calculated as $\nu = 0.0.49999925$.

4.2.3.2 Nonlinear elastic material

The nonlinear elastic material node provides a nonlinear addition to the linear elastic material node described over. The node is used to model stress-strain relationships which are nonlinear even at infinitesimal strains[44]. As breast tissue has a nonlinear elastic behaviour under ultrasound transmission, it could provide benefits modelling the tissue by this node. However, to use the nonlinear elastic material node reference values for stress and strain of the material are necessary, as well as a stress exponent. For the research in this thesis, it was considered satisfying using the linear elastic material node to discuss whether oscillations of the microcalcification trigger SURF detection.

4.2.4 Body load

A body load is a way of adding volumetric loads in a domain. The microcalcification and the breast tissue are modelled as two different domains. The default of the Body load node is Force per unit volume, which is the same unit as the radiation force generated in Wavesim. The radiation force by a SURF pulse is therefore applied as a body load on both domains. For stationary solutions, the body load is constantly applied on the microcalcification domain only. For investigations of the effect of scattering based radiation force, both a body load on the whole domain and one on the microcalcification domain only are chosen. The equation for body load is from Newtons 2nd, S is the stress applied and F_V is the volume force, as[44]

$$\rho \frac{d^2u}{dt^2} = \nabla \times S + F_\mathrm{V}. \tag{4.4}$$

4.2.4.1 SURF radiation force profiles in COMSOL

Figures 4.7 and 4.8 show the imported force field generated in Wavesim in COMSOL by 2D visualisation from sideways and above. The radiation force is applied as a body load in COMSOL. The radiation force is imported from the azimuth field in Wavesim. The profile without apodization is considered a realistic SURF pulse. Compared to figure 4.3 of the onaxis radiation force, the azimuth radiation force in figure 4.7 has its maximum in 11 mm depth, but for the onaxis profile the maximum is in 18 mm depth. Because of no apodization, edge waves are observed at 11 mm depth, increasing the amplitude of radiation force at this depth in radial directions.

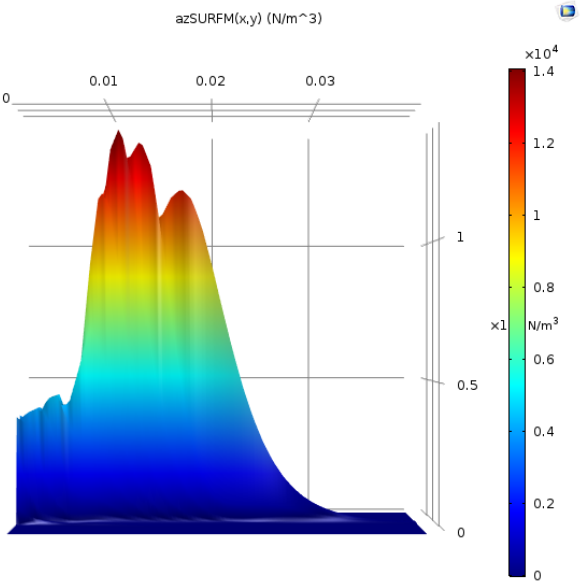

Figure 4.7: A SURF force profile visualized from the side in COMSOL.

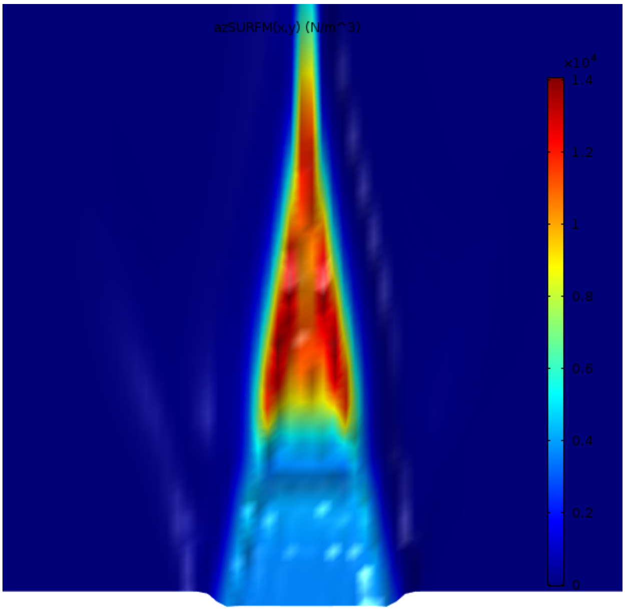

Figure 4.8: A SURF force profile visualized and zoomed in from above in COMSOL.

4.2.4.2 Step-function

For dynamic simulations, the body load is applied in a limited time, to simulate the period of the induced radiation force by a SURF pulse. A smooth step-function is made by an analytic function in COMSOL to make sure of the duration of induced radiation force. The step-function is valued ~ 1 for a limited time denoted t_{on} and zero elsewhere. t_{on} is calculated as $t_{\mathrm{on}} = 2{\cdot}T_{\mathrm{HF}} = 2{\cdot}1/f_{\mathrm{HF}}$, where T_{HF} is the pulse period of a HF pulse. Figure 4.9 shows the body load applied to the center of the microcalcification for three transmitted SURF pulses with $\mathrm{PRF} = 14\,\mathrm{kHz}$. This is seen as a body load applied at $t = 0\,\mu\mathrm{s}$ and repeated two times in a period of $1/\mathrm{PRF} \approx 71\,\mu\mathrm{s}$. The radiation force is applied in all points at the same time. The step function could be modified to be applied in different times in each depth. However this is insufficient, as the period of shear displacement is many times longer than t_{on}.

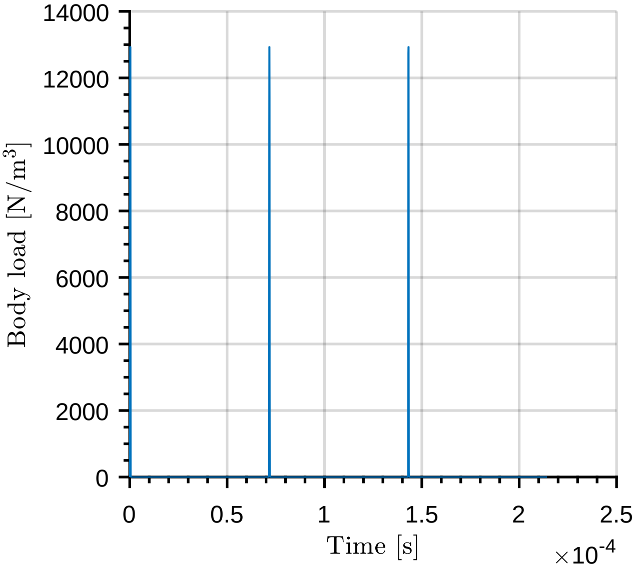

Figure 4.9: A step function controls the body load applied to the microcalcification and tissue domains.

4.2.5 Initial Values

The initial value is a specified value of an unknown function at a specific time $t = t_0$, in the model of the breast tissue the initial values apply for displacements of all points at $t = 0$. Given the initial displacement values, the PDE becomes an initial value problem and is solved as an evolution from the initial values. When building the solid mechanics model, the initial values for all domains, displacement field and structural velocity field, are zero[44]

$$\mathbf{u} = 0 \quad \frac{du}{dt} = 0. \tag{4.5}$$

4.2.6 Axial symmetry

For all axisymmetric components modelled in 1D or 2D in COMSOL, the Axial Symmetry node is the default, and the boundary condition is active on all boundaries on the symmetry axis[44]. The cylindrical coordinates axes are radial and vertical $(r, z) \geq 0$. z is the depth of the medium, and r is the width. By using symmetries in a model the computation size and much memory are reduced by one-half or more, which should be considered when solving large problems in COMSOL. A 3D problem may then be solved as a 2D problem in the rz-plane and variations in the angular direction φ are not to be considered[47].

4.2.6.1 Axisymmetric geometry of breast tissue with a microcalcification embedded

Figure 4.10 shows the axisymmetric 2D geometry modelled in COMSOL, one big tissue domain and one small domain for the microcalcification. The geometry is visualised with the mesh, a term to be further presented. The mesh is most dense at the microcalcification domain. In figure 4.11, the geometry is zoomed around the microcalcification modelled as a semicircle with 100 µm radius centered at $(r, z) = (0, 20)$ [mm]. The surrounding tissue is modelled by 10 mm depth and 5 mm width centered at $(r, z) = (2.5, 20)$ [mm]. The domain of the surrounding tissue is reduced to make the computational size in COMSOL smaller, but the displacements of a microcalcification are certain to be within the geometry.

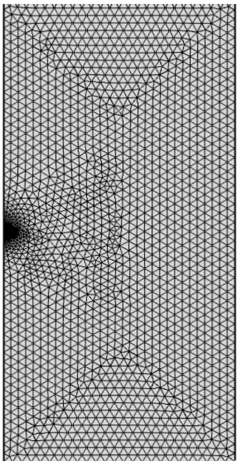

Figure 4.10: The geometry of a microcalcification embedded in tissue with mesh build.

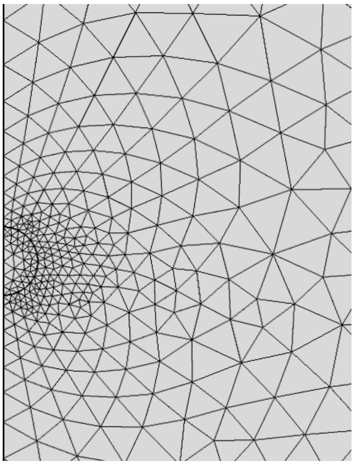

Figure 4.11: The geometry zoomed of a microcalcification embedded in breast tissue.

4.2.7 Low-reflecting boundary

The low-reflecting boundary node is used to make sure the shear- and pressure waves propagate out from the model without reflection in a time-dependent analysis. With this node, the computational domain can be reduced to a practical size. As a default, the low-reflecting boundary module takes material data from the domains in the model and makes a perfect impedance match for both pressure waves and shear waves. The module is based on the following equations

$$\sigma \cdot \mathbf{n} = -\mathbf{d}_{\mathrm{im}} \frac{d\mathbf{u}}{dt} \quad \mathbf{d}_{\mathrm{im}} = \mathbf{d}_{\mathrm{im}}(\rho, c_{\mathrm{s}}, c_{\mathrm{p}}). \tag{4.6}$$

The mechanical impedance $\mathbf{d}_{\mathrm{im}}$ is a diagonal matrix with identity matrix $\mathbf{I}$ as

$$\mathbf{d}_{\mathrm{im}} = \rho \frac{c_{\mathrm{p}} + c_{\mathrm{s}}}{2} \mathbf{I}. \tag{4.7}$$

In the model of breast tissue, the Low-reflecting boundary node is assigned to the boundaries of the tissue domain such that the pressure- and shear-waves propagate out from the tissue. The damping type can be chosen between standard "Pressure and Shear waves" and "User-defined"[44]. The standard type was first used. During this thesis, its efficiency was suspected, as the simulated displacements had confusing oscillations. The pressure waves are considered to be submissive in the displacement compared to the shear waves. Equation 4.7 is the average between the pressure and shear impedance, which may not be an optimal impedance for absorbing any of the waves at the boundaries. The mechanical impedance in the low-reflecting boundary is therefore calculated to make sure all shear waves are absorbed in the boundaries, and the pressure waves are neglected. The mechanical impedance at the boundaries is calculated as

$$\mathbf{d}_{\mathrm{im}} = \rho c_{\mathrm{s}} \mathbf{I}. \tag{4.8}$$

4.2.8 Free node

When the physics interface is added, COMSOL automatically generates the Free node, which is the default boundary condition. This node makes sure no constraints or loads are acting on the boundaries. As other nodes are added on the boundaries, the free node is overwritten on the current boundary[44].

4.2.9 Finite Element Analysis

Finite Element Analysis (FEA) is software for solving field problems by a numerical approach, which is utilised by COMSOL. The purpose is to reduce the number of experiments to be run when modelling a system. A physical system and its behaviour are often described by a set of equations, where the systems boundary conditions and geometry govern the equations. The equations describing a system are usually in the form of partial differential equations (PDE), characterised by unknown variables and their partial derivative. The foundation of FEA software is constituted by the laws of physics expressed in mathematical models, consisting of different conservation laws, laws of classical mechanics, and laws of electromagnetism[48].

The mathematical models are discretised by the Finite Element Method (FEM). This method uses numerical approaches in solving PDEs. A large problem is subdivided into smaller and simpler parts called finite elements. The solution to PDEs is in the form of dependent variables, which can be velocity fields, temperature fields and structural displacements. In the FEM-model in this thesis, the dependent variables are structural displacements. The solutions are found in space and time. In Solid mechanics, the physicals descriptions by FEM are based on the balance of forces and the relations between stresses to strains, such as Hooke's law[48]. In this thesis, FEM is chosen as the preferred numerical method as it is considered an effective and accurate method for simulating wave propagations[49].

4.2.9.1 Time dependent analysis

Solving time-dependent problems such as waves causes further complexity in the calculations. Time dependence demands further integration and interpolation in time to the initial computation. The accuracy of a model is limited by how well the finite element mesh resolves the waves in space and how well the time step resolves the temporal variations. The convergence of the solution of a time-dependent problem is highly dependent on the geometric scale of the physics problem as well as the time scales of the different domains.

In FEA the wave equations are solved in the time domain, for an accurate solution the time step is chosen carefully. The material properties in all domains govern the mesh size needed, as the material parameters govern the shortest possible wavelength. As a minimum, the mesh must fulfil the Nyquist criterion, such that in each domain there are at least two elements, N, per local wavelength, but in practice, it is advised to choose N as

$5 \leq N < 10$. The minimal element size $h_{\min}$ should be chosen as

$$h_{\min} \leq \frac{\lambda}{N} = \frac{c}{f_{\max}}. \tag{4.9}$$

$f_{\max}$ is the maximum frequency content in the excitation, and c is the highest wave speed in the material. The meshing used in the model is illustrated in figure 4.10, where the meshing size varies for the different domain sizes. The Courant-Friedrich-Lewy (CFL) number is introduced to guide the time step sizing. The CFL-number is recommended to be chosen as $\mathrm{CFL} \leq 0.2$ for insurance of convergence in the solution of PDE. A CFL number of 0.1 is proved to be near optimal. The time step should resolve the wave as good in time as the mesh does in space. Increasing the time step will not make optimal use of the mesh, decreasing the time step will only lead to longer solution time without improving the result. CFL is related to the timestep Δt through

$$CFL = \frac{c\Delta t}{h_{\min}}, \tag{4.10}$$

solved for Δt and equation 4.9 inserted[49]

$$\Delta t = \frac{CFL}{N \cdot f_{\max}}. \tag{4.11}$$

4.2.10 Modelling with a Gaussian

A Gaussian force field has been used in understanding and confirming the behaviour of the elastic system modelled in COMSOL. As seen in figure 4.7, a SURF pulse with no apodization consists of edge waves. The profile of the radiation force induced by a SURF pulse may lead to gradients difficult to anticipate. A Gaussian can be modelled with practical dimensions by

$$F = F_0 e^{(-((z - z_{\mathrm{focus}})^2)/\sigma_{\mathrm{z}})} e^{(-((r - r_{\mathrm{focus}})^2)/\sigma_{\mathrm{r}})}, \tag{4.12}$$

where F_0 is chosen to be of the same absolute value as for a typical radiation force from a SURF pulse, $\sim 13\,000\,\mathrm{N/m^3}$. The focus in radial and vertical coordinates are chosen by r_{focus} and z_{focus}. The pulse width in radial and vertical directions are chosen by σ_{r} and σ_{z}. The Gaussian was chosen narrow in radial width to provide an understanding of the dimensions of the radiation force induced by a SURF pulse. The pulse made is similar to the smooth shape of an one element circular transducer. The force profiles are generated in Matlab and interpolated to COMSOL like the SURF pulses in Wavesim. In 2D the force profile is visualized in COMSOL as in figures 4.13 and 4.12.

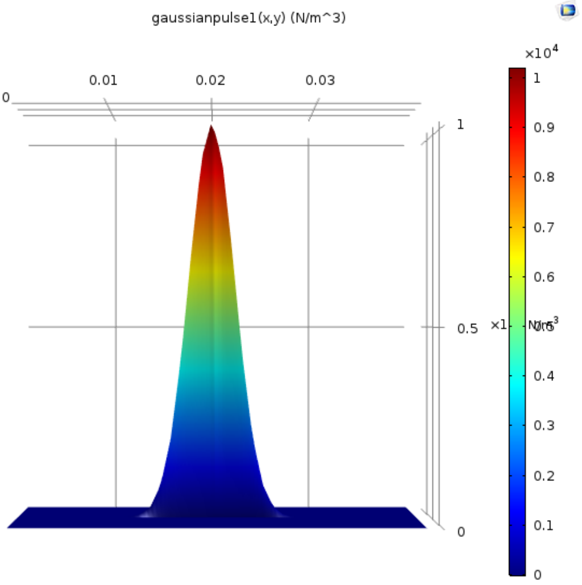

Figure 4.12: A Gaussian force profile visualized from the side in COMSOL.

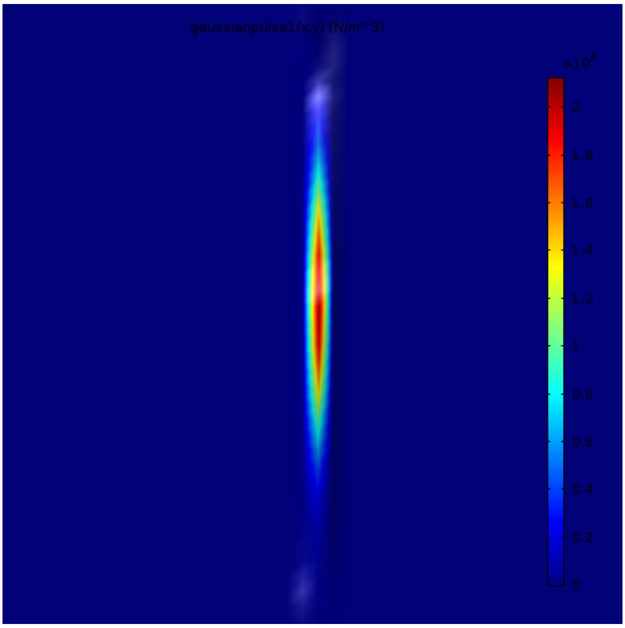

Figure 4.13: A Gaussian force profile visualized from above in COMSOL.

Chapter 5

Analysis

This chapter presents the results of the simulations and experiments performed in this thesis. The results are analysed and discussed within the theoretical framework presented in chapter 2, 3 and 4. The first section describes simulations on a single or multiple ultrasound pulses transmitted in a limited time. The behaviour of the elastic system under dynamic conditions is after that discussed. The next section presents the simulations performed by applying a force constantly on the microcalcification only to find a stationary solution of the displacement induced. The results are compared to the Stokes drag force. In the third section, the effect of varying specific material parameters is discussed. The next section presents results from experiments on B-flow twinkling and SURF detection on a breast-mimicking phantom. A discussion at the end of this chapter is provided to structure and further discuss the most important findings during the analysis.

5.1 Dynamic displacement simulations

This section presents the displacement simulations performed for ultrasound pulses transmitted in a limited period t_{on}, and concerns both a single pulse and multiple pulses transmitted. The force from a SURF pulse generated in Wavesim is considered to be complex as it consists of edge waves and possibly unpredictable gradients. Therefore, the displacements induced by a smooth Gaussian is first presented. Hopefully, this provides an intuitive understanding of the elastic behaviour of breast tissue with an embedded microcalcification, before analysing displacements induced by a more complex SURF pulse. First, the displacement of a microcalcification by transmitting a single pulse is discussed. After that, the microcalcification is replaced with tissue such that the resulting displacement in homogeneous breast tissue is used in a comparison. The effect of scattering is analysed by applying an extra force to the microcalcification domain only besides. Next were three SURF pulses transmitted in a period decided by the Pulse Repetition Frequency (PRF). The same situation is performed with three LF pulses. The PRF is then modified by analytic expression to trigger oscillations of the microcalcification possibly.

5.1.1 Dynamic displacements induced by a Gaussian

The Gaussian force profile described in section 4.2.10 is used in simulations to provide an intuitive understanding of the elastic behaviour of breast tissue with an embedded microcalcification. In figure 5.1 the displacement of a microcalcification induced by a Gaussian pulse transmitted in $t_{\mathrm{on}} = 2 \cdot \frac{1}{f_{\mathrm{HF}}} = 0.25\,\mu\mathrm{s}$ is presented. The microcalcification is moved $\sim 0.26\,\mathrm{nm}$ before going back to its initial position. The duration of the shear displacement T_{s} is analytically calculated as $T_{\mathrm{s}} = 2 \cdot \frac{R_{\mathrm{s}}}{c_{\mathrm{s}}} = 2 \cdot \frac{1\,\mathrm{mm}}{1.8172\,\mathrm{mm/ms}} \approx 1.1\,\mathrm{ms}$. $R_{\mathrm{s}} \approx 1\,\mathrm{mm}$ is the dimension of the force when it is considered to be of practical dimensions[28]. The shear-wave velocity c_{s} in breast tissue is calculated in COMSOL by the density and shear modulus of the material via the relation $\mu = \rho c_{\mathrm{s}}^2$. The analytically calculated period of the shear displacement agrees quite good with the simulated displacement period in figure 5.1, such that the Gaussian radiation force is of practical dimensions in this research.

In figure 5.2 the microcalcification domain is replaced with breast tissue such that the tissue is homogeneous. The displacement is shown together with the displacement of the microcalcification in figure 5.1. The displacement amplitude is only increased $\sim 0.02\,\mathrm{nm}$ and the displacement fluctuation is $\sim 23\,\mu\mathrm{s}$ faster. The microcalcifications impact on the displacement is dampening, as its material properties are heavier and stiffer than the surrounding tissue as in table 4.3. The change in displacement in the homogeneous breast tissue is still minor. The tissue displacement is seen as the major factor of displacement.

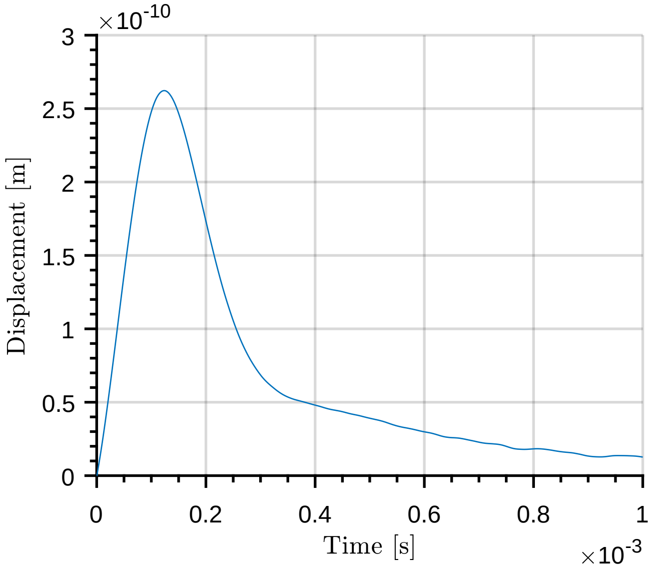

Figure 5.1: The displacement of a microcalcification induced by a Gaussian.

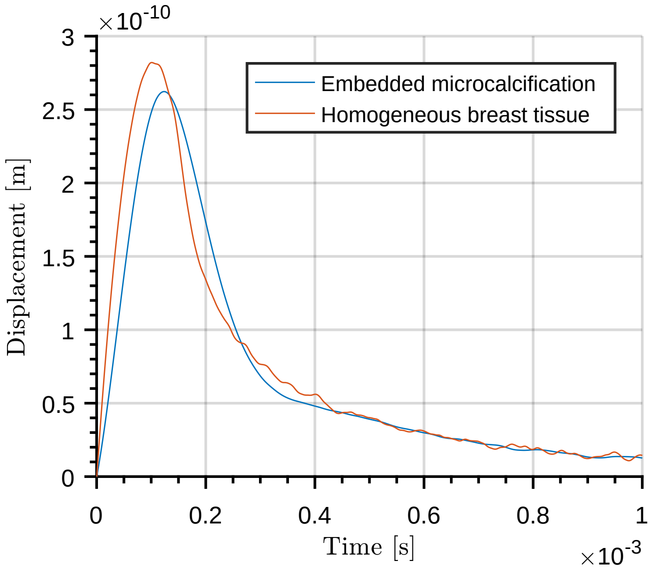

Figure 5.2: The displacement of a homogeneous breast tissue induced by a Gaussian shown together with the microcalcification displacement.

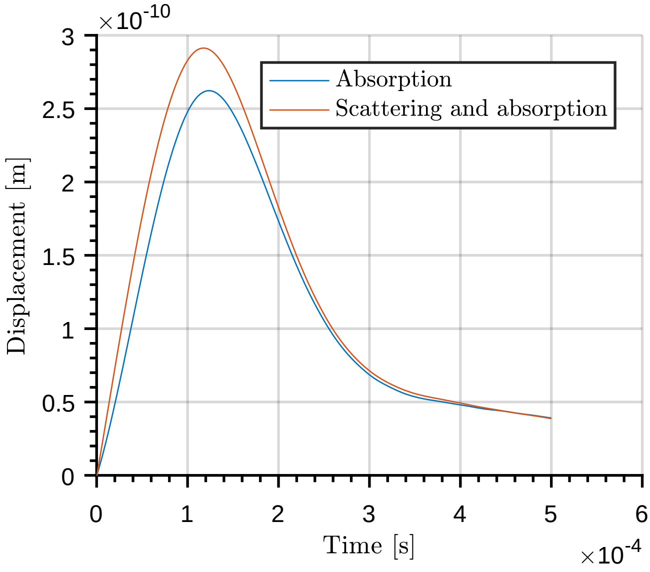

Figure 5.3: The displacement of a microcalcification with an extra scattering force induced by a Gaussian.

A particle or an object embedded in the tissue will scatter a transmitted ultrasound pulse. Therefore, there will also be radiation force induced due to scattering besides radiation force from absorption. The Gaussian force is applied to the entire domain as in figure 5.1, as well as on the microcalcification domain only besides. The scattering radiation force is therefore applied with the same value as the radiation force from absorption. The increase in displacement is as seen in figure 5.3, an increase of $\sim 0.03\,\text{nm}$, compared to the displacement induced by applying only absorption radiation force on the entire domain. In reality, scattering radiation force on the same size as radiation force from absorption is unlikely, Lu[50] calculated the scattering force from a microcalcification numerically in COMSOL to be much smaller than the absorption radiation force. The simulation gives an understanding of how large a radiation force by scattering must be to make a significant impact on the displacement of a microcalcification particle. The result tells that scattering radiation force makes a minor impact on the induced displacement of a microcalcification in the case of a Gaussian.

5.1.2 Dynamic displacements induced by a SURF pulse

A single SURF pulse is transmitted in one period, $t_{\text{on}} = 2 \cdot 1/f_{\text{HF}}$, on a breast tissue with a microcalcification embedded. The resulting displacement curves for the microcalcification centered at $(r, z) = (0, 20)$ [mm] and the tissue point at the coordinates $(r, z) = (0, 16)$ [mm] are seen in figure 5.4.

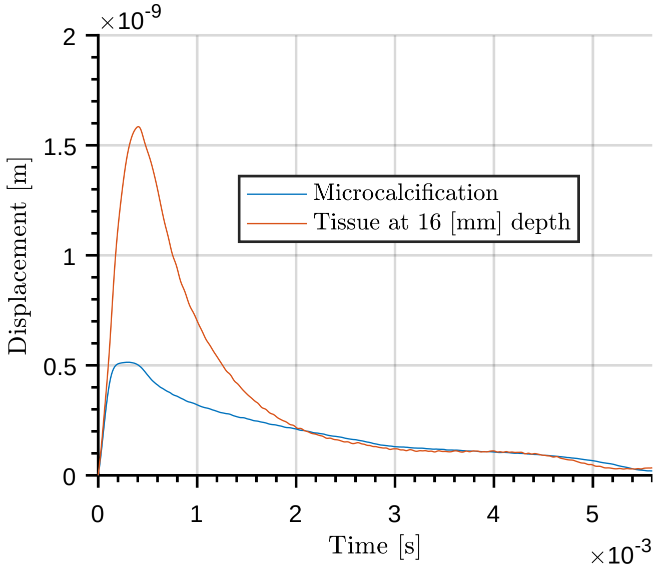

Figure 5.4: The displacement of a microcalcification induced by a single SURF pulse.

The microcalcification is moved $\sim 0.5\,\text{nm}$ before going back to its initial position, whereas the tissue point is experiencing a displacement of $\sim 1.6\,\text{nm}$. The period of shear displacement T_{s} for the two points, is the same. The onaxis radiation force in figure 4.3 has its maximum in 18 mm depth. The radiation force is applied such that the microcalcification experiences this peak, as a transmitted SURF pulse is focused in the typical depths of a microcalcification. Figure 4.8 shows the occurrence of edge waves in a SURF pulse without apodization. Therefore, a higher radiation force is experienced by other points in the tissue, leading to larger displacement experienced by the tissue at 16 mm depth. The behaviour of breast tissue has similarities to the behaviour of an elastic mass-spring system. Hooke's law describes the linear elastic material node in COMSOL as in equation 4.2. Larger radial and vertical dimensions of the radiation force induced lead to more mass contribute to the triggered shear displacement. The dimensions of the radiation force induced by a SURF pulse lead to expanding of the displacement fluctuation compared to the displacement induced by a Gaussian in figure 5.1. Shear waves are generated in more source points in the breast tissue. Small sources in the breast tissue appear as an extended source with different source points such that the shear displacement duration is expanded for a SURF pulse.

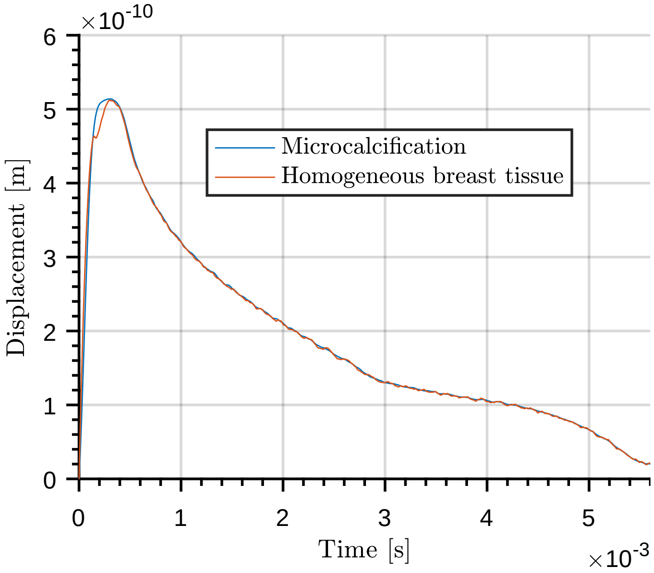

Figure 5.5: The displacement of homogeneous breast tissue compared to a microcalcification in $(r, z) = (0, 20)$ [mm] induced by a SURF pulse.

SURF detection of microcalcifications is based on detecting generated differences in an image of breast tissue. B-flow imaging detects flows. To explore if radiation force-induced displacement of a microcalcification triggers SURF detection a homogeneous breast tissue is considered. The displacement of homogeneous breast tissue is in figure 5.5. The displacement of homogeneous tissue is shown together with the microcalcification displacement from figure 5.4. The tissue point is at $(r, z) = (0, 20)$ [mm], the same coordinates as the microcalcification centre in figure 5.4. The same radiation force is experienced in the homogeneous tissue point. The displacements are so similar that the displacement from the surrounding tissue is understood as the major factor of the displacement experienced by a microcalcification in figure 5.4, the microcalcification tends to have a minimal impact on the SURF pulse induced displacement. This result is confirmed by the findings with a Gaussian, as even with a narrow radiation force the presence of the microcalcification tends to be of minimal relevance in the resulting displacement. The hypothesis suggesting SURF detection of microcalcifications triggered by oscillations of the particles seems unlikely with this result unless radiation force from scattering on the microcalcification has an important impact. The same applies to the B-flow twinkling as the twinkling would occur other places in the tissue as well, and not around or on the surface of a microcalcification only. Compared to the size of the surrounding tissue, the microcalcification is too small to be prominent in the generated displacement.

The procedure of addressing the possible effect of radiation force from scattering by a SURF pulse is performed in the same way as for the Gaussian. It is shown in section 2.4.1 how this can be calculated. Figure 5.6 shows the radiation force being distributed twice to the microcalcification domain compared to the tissue 0.5 mm behind in depth. Such a situation is as discussed in section 5.1.1 unlikely. The simulation is provided to give an idea of how large the radiation force from scattering must be to make an impact for a SURF pulse.

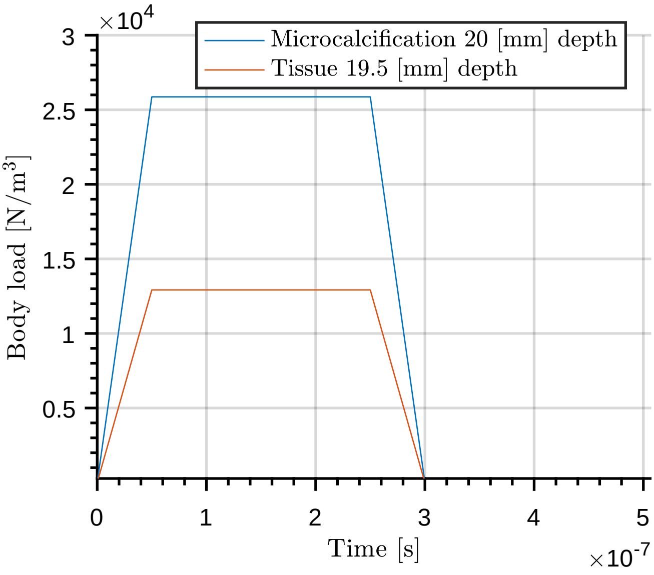

Figure 5.6: The distribution of radiation force on the microcalcification and on the tissue with scattering radiation force besides, both at the axis $r = 0$.

The effect was shown to be minimal as in figure 5.7. The displacement decreased when adding an extra force to the microcalcification domain only. This result is confusing, applying an extra radiation force on the microcalcification dampens the displacement as the microcalcification has heavier material properties. The increment of $\sim 5\%$ in the same investigation with a Gaussian in figure 5.3 is considered more realistic. The effect of scattering radiation force is considered to be of much less significance than the one of absorption. The findings in the relations of tissue and microcalcification sizes apply for scattering radiation force as well. As scattering radiation force is shown to be of minor importance, displacement of microcalcification induced by ultrasound radiation force is concluded not to be triggering SURF detection or the twinkling in B-flow imaging.

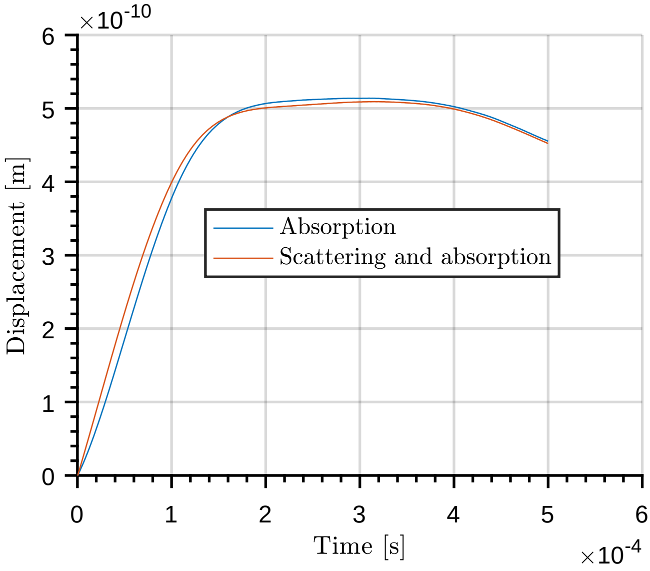

Figure 5.7: A comparison of the displacement of the microcalcification with and without an added scattering radiation force the first 500 µs.

Shear waves generated by the radiation force applied on the tissue result in displacements in areas where the SURF pulse is not focused. The displacements in radial and vertical directions are controlled in figures 5.8 and 5.9 in the tissue point $(r, z) = (2.5, 20)$ [mm], the same depth as the microcalcification. The experienced radiation force at this point is 50 N/m^3. Because of the axisymmetry in the COMSOL-model, the microcalcifications centre does not experience variations in radial direction as it is centred at $r = 0$, where the boundary conditions for axisymmetry apply. The θ in equation 2.44 contributes in the displacements. The angle in $(r, z) = (2.5, 20)$ [mm] is different compared to the microcalcification at the axis where the radiation force is focused. However, the impact of the angle θ is not fully understood.

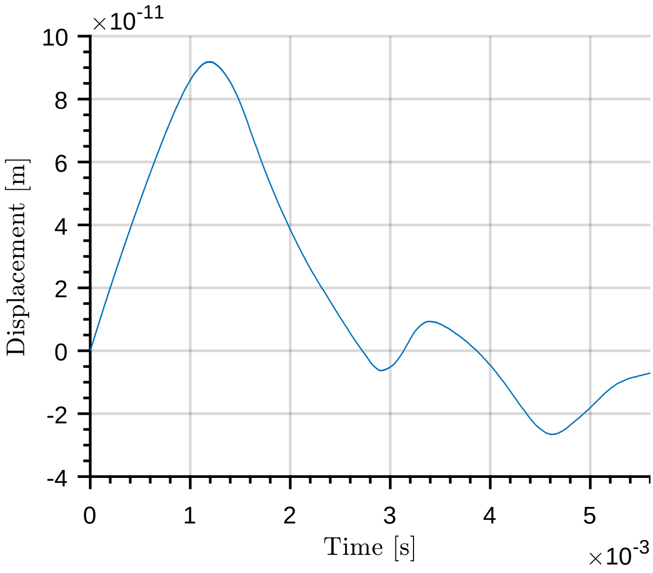

Figure 5.8: The displacement in r-direction in tissue-coordinates $(r, z) = (2.5, 20)$ [mm] induced by a SURF pulse.

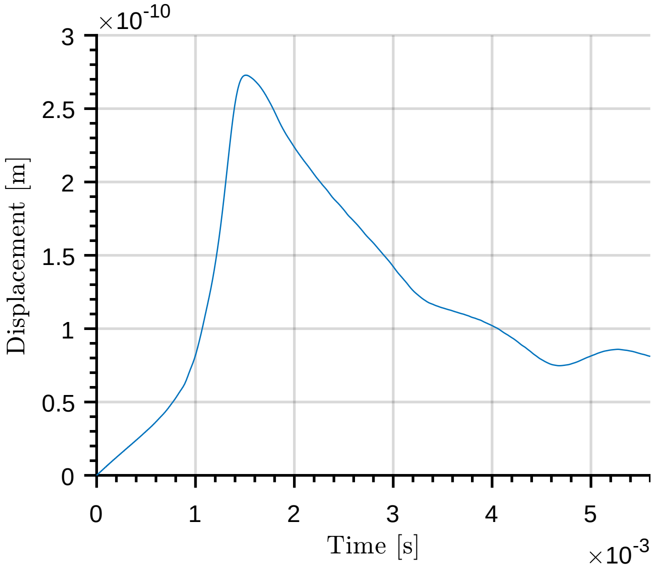

Figure 5.9: The displacement in z-direction in tissue-coordinates $(r, z) = (2.5, 20)$ [mm] induced by a SURF pulse.

5.1.3 Dynamic displacements induced by three SURF pulses

Simulations were performed by transmitting three SURF pulses on the entire tissue, a situation realistic for an ultrasound scanner. In figure 5.10 three pulses are transmitted with a PRF of 14 kHz. The microcalcification displacement the first $\sim$ 70 µs does not have a concave shape as expected. However, the displacement of the tissue at depth $z = 19$ mm, 1 mm behind the microcalcification has a concave shape. Figure 5.10 further contributes to the theory that the tissue displacement is the dominant factor, and the figure illustrates how the tissue pushes and further accelerates the microcalcification from behind.

Figure 5.11 shows three SURF pulses transmitted into homogeneous breast tissue. The tissue at 20 mm depth is following the tissue at 19 mm for the first two pulses. The tissue displacement is larger for the third pulse at 19 mm due to higher radiation force. At the start of the induced displacement, the microcalcification in figure 5.10 dampens its displacement. After a long period as in figure 5.4, the displacement will be dominated by the tissue displacement.

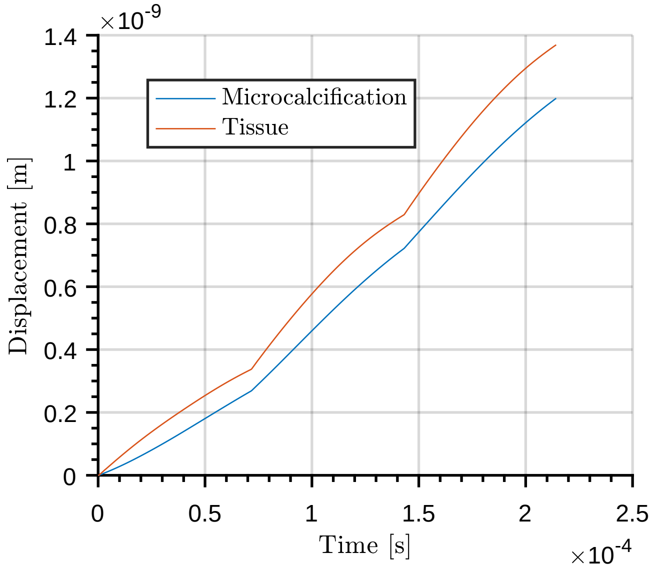

Figure 5.10: The displacement induced by three SURF pulses transmitted with a PRF of 14 kHz. The microcalcification is positioned at $(r, z) = (0, 20)$ [mm] and the tissue point is at $(r, z) = (0, 19)$ [mm].

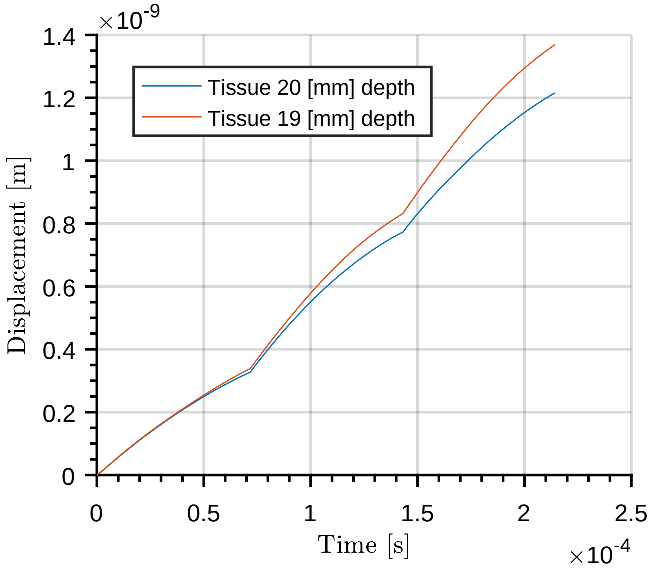

Figure 5.11: The displacement of a homogeneous breast tissue at $(r, z) = (0, 20)$ [mm] induced by three SURF pulses transmitted with a PRF of 14 kHz.

5.1.4 Dynamic displacements induced by three LF pulses

Three pulsed simulations were also performed with a LF pulse, where the pulse period is five times the period of a SURF pulse, $t_{\mathrm{on}} = \frac{1}{f_{\mathrm{LF}}}$. This is chosen to simulate the contribution from the LF pulse before the HF pulse is typically positioned on the top of the LF pulse in a SURF pulse complex. The displacement curves in figures 5.10 and 5.12 are similar in shapes. The magnitude of the displacement of a microcalcification induced by a LF pulse compared to a SURF pulse, $\sim$ 3 times smaller, even though the pulse period is five times longer. The contribution of a LF pulse in the displacement is not the triggering factor of SURF detection of microcalcifications.

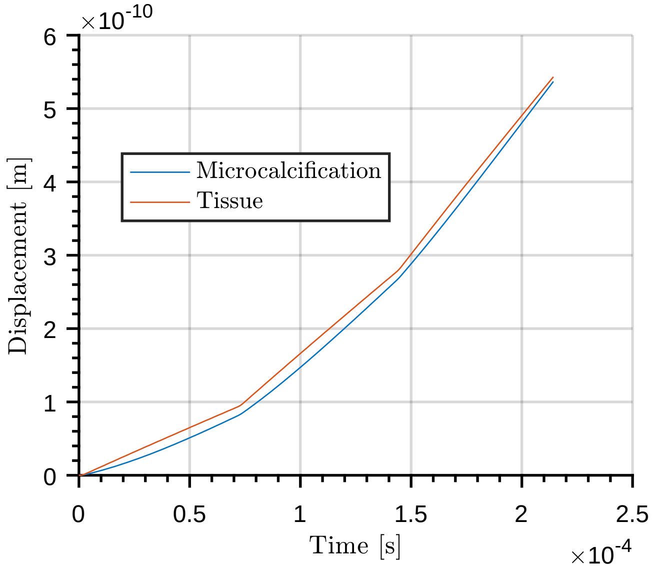

Figure 5.12: The displacement induced by three LF pulses transmitted with a PRF of 14 kHz. The microcalcification is positioned at $(r, z) = (0, 20)$ [mm] and the tissue point is at $(r, z) = (0, 19)$ [mm].

5.1.5 Lowering the PRF to trigger oscillations of the microcalcification induced by multiple SURF pulses

To possibly trigger resonance-like behaviour of the microcalcification the PRF was modified by the analytic calculation in equation 2.55. For the material parameters in table 4.3, the shear wave velocity $c_\mathrm{s} = 1.8172\,\mathrm{m/s}$, $\mathrm{PRF} \approx 5\,\mathrm{kHz}$ for a microcalcification of radius $100\,\mu\mathrm{m}$. The result is seen in figure 5.13. The radiation force induced by a SURF pulse is transmitted only on the microcalcification domain in a time $t_\mathrm{on} = 0.25\,\mu\mathrm{s}$, and transmitted every $t = \frac{1}{\mathrm{PRF}} \approx 200\,\mu\mathrm{s}$. In [17] it was assumed that one of the two considered types of Twinkling Sign Artifacts was periodic oscillations of microcalcifications induced by radiation force. However, oscillations were not observed in experiments for any PRFs. The oscillations in figure 5.13 were triggered by applying the force only on the microcalcification. Radiation force applied to the tissue, besides, would trigger tissue displacements, and expand the fluctuation of the microcalcification displacement. The oscillations of a microcalcification in an experiment requires a very narrow focused ultrasound pulse such that only the microcalcification is experiencing radiation force, a situation which is unrealistic. In the displacement simulations, the viscous component of shear visco-elasticity is not included, which in reality will limit the displacement-amplitudes of both a microcalcification and the surrounding tissue. Radiation losses limit the displacement amplitudes in simulations, the analytic calculation for the losses is started but not concluded with simulations yet.

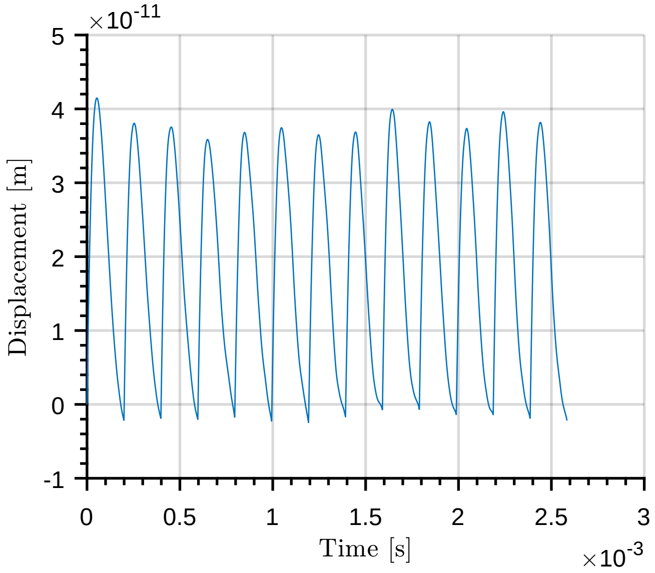

Figure 5.13: An oscillating behaviour of a microcalcification is triggered by multiple SURF pulses transmitted with a modified PRF of $\sim$ 5 kHz.

5.2 Stationary displacement solutions

Applying a constant force on the microcalcification domain only was performed to find a stationary solution of the displacement of a microcalcification. A stationary solution could provide an agreement with the Stokes drag force and give a physical understanding of the elastic system. A constantly applied ultrasound radiation force is not a realistic situation. The radiation force constantly induced on the microcalcification is calculated by the formula in equation 2.27. The absorption coefficient for breast tissue used is $\alpha_{\mathrm{e}} = 16.11 \cdot 10^{-6}$ (mMHz)$^{-1}$, where f is chosen as the HF frequency. Figure 5.14 shows the stationary displacement simulated for a microcalcification when mechanical index $\mathrm{MI} = 2$. The dotted line is the displacement calculated by Stokes drag force in equation 2.49, for a microcalcification of radius 100 µm and shear modulus μ of the breast tissue as in table 4.3. The simulated stationary displacement provides an agreement with the Stokes drag force. Before the microcalcification reaches its stationary solution, the displacement experiences an overshoot.

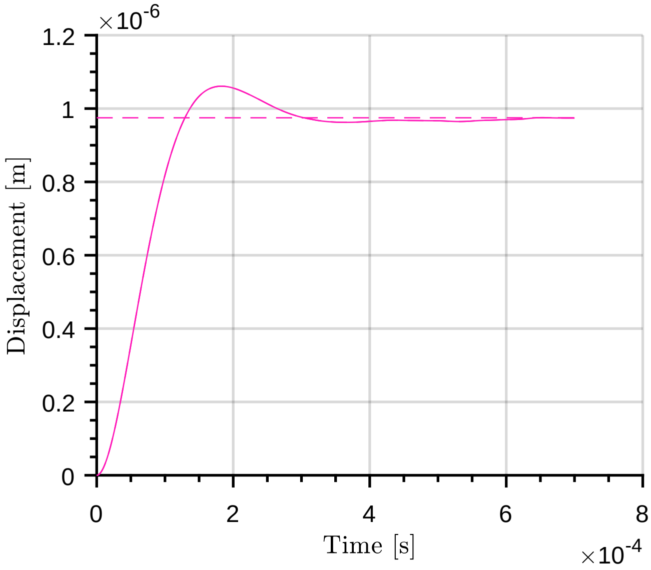

Figure 5.14: The stationary simulated displacement for a radiation force constantly applied on the microcalcification with $\mathrm{MI} = 2$. The calculated displacement by Stokes drag force is the dotted line.

In simulations, the mechanical index MI is varied to make sure the stationary simulations provide an agreement to Stokes drag force for multiple radiation forces. Figure 5.15 shows the relative error between simulated displacement Ψ and the analytic displacement by the Stokes drag force $\hat{\Psi}$ in dB unit. The relative error is calculated as $20log(|1 - \frac{\hat{\Psi}}{\Psi}|)$. The relative error is highest in when $\Psi = \hat{\Psi}$, which is controlled by the crossing of the simulated displacement and the analytic displacement in figure 5.14. As the solution in COMSOL is solved numerically, this does not occur at all times. The relative error for $\mathrm{MI} = 2$ differs from the other MIs for t = 0.4 ms to 0.6 ms. The displacement is largest for $\mathrm{MI} = 2$, leading to fewer decimals in the solution matrices generated in COMSOL, which makes the solution more precise. The different MIs are still from this concluded to be linearly related, which confirms the linearity in the elastic model. The Stokes drag force applies for all MIs. With these findings, it is clear that the displacement of a microcalcification increases linearly with increasing radiation force. This explains how the radiation force-induced displacement of a microcalcification by a LF pulse is smaller than the displacement induced by a SURF pulse.

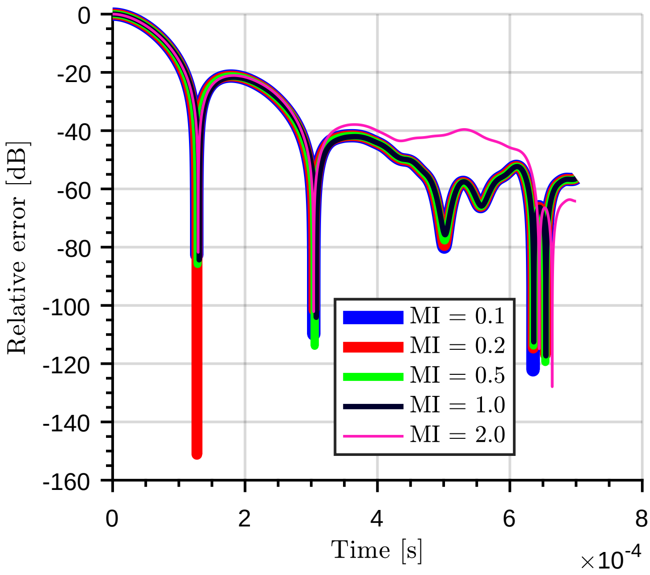

Figure 5.15: The relative error in simulated stationary displacement compared to the displacement by Stokes drag force for different MIs.

In figure 5.16 the force $F(t)$ is transmitted in a time t on the microcalcification domain only, with duration such that all points on the microcalcification of radius a contributes in maximum shear displacement Ψ. The radiation force applied is the same as in figure 5.14, $\mathrm{MI} = 2$. The rectangular time t is chosen to be long enough to reach the stationary solution, such as $t > 2a/c_\mathrm{s}$. To make this certain the time is chosen as $t = 4 \cdot a/c_\mathrm{s} \approx 220\,\mu\mathrm{s}$. The displacement will therefore increase over half the period $t/2$, before being approximately constant over the next interval of $t/2$, and decrease back to the initial position at the next interval $t/2$. In figure 5.14 the displacement experienced an overshoot before reaching the stationary solution. In figure 5.16 the force is removed before this occurs, but the displacement of the microcalcification is having an undershoot at $t = 0.37\,\mathrm{ms}$ before going back to its initial position. The undershoot and the overshoot are close to each other in values.

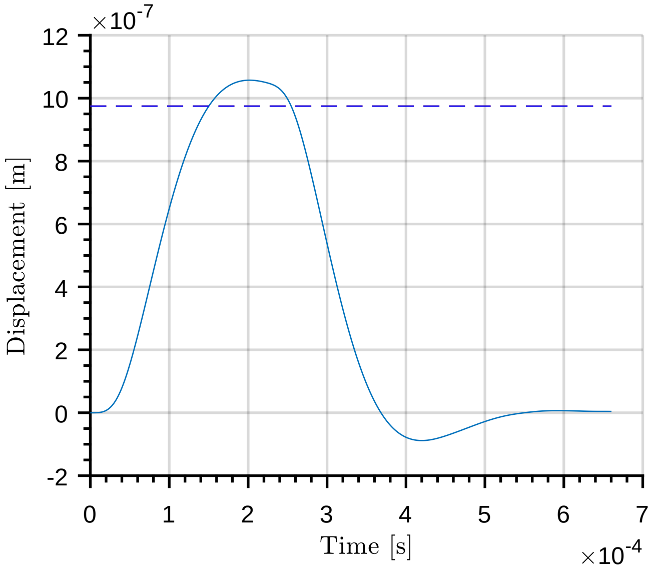

Figure 5.16: The displacement of a microcalcification pulsed in $t = 220.12\,\mu\text{s}$ to the stationary solution, the displacement by Stokes drag force is the dotted line.

5.3 Effect of varying specific material parameters

The analysis in this section is provided to investigate the effect of varying some specific material parameters of both the surrounding tissue and the microcalcification. The properties are investigated in stationary simulations, as it is considered easier to point out physical properties.

5.3.1 Varying the shear stiffness of the breast tissue

As the stiffness of breast tissue varies between healthy, benign and malignant breast tissue, simulations were done experimenting on the shear modulus of the breast tissue. Existing quantitative literature concludes with Young's modulus varying as $\sigma = 0\,\text{kPa}$ to $180\,\text{kPa}$, between healthy, benign and malignant breast tissue[51]. The Young's modulus can be approximated as $\sigma \approx 3\mu$, such that the variation of the tissue types in shear stiffness is $\mu = 0\,\text{kPa}$ to $60\,\text{kPa}$. Figure 5.17 shows the stationary displacement for a radiation force F decreasing with $\frac{1}{\mu}$ with increasing values of shear modulus. The dots are the stationary displacements simulated for each shear modulus μ. Equation 2.49 confirms, as solved for Ψ will have the shear modulus in the numerator. The red line is the analytic displacement by Stokes drag force.

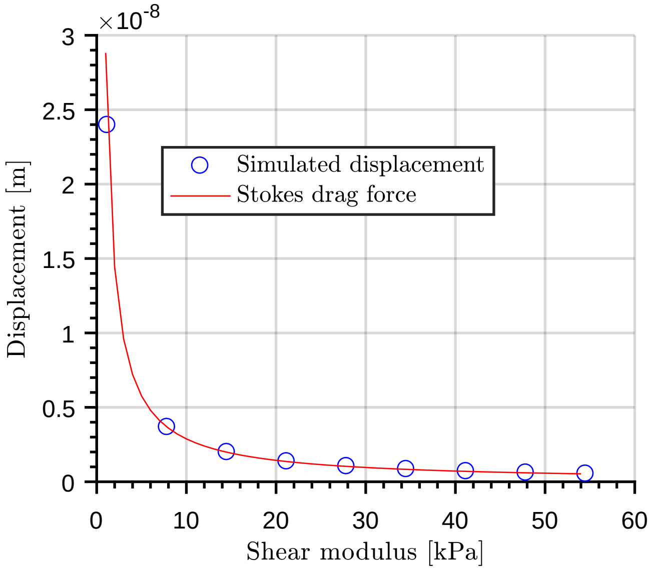

Figure 5.17: The stationary displacements for a microcalcification when the shear modulus is varied from 1.2 kPa to 54 kPa with a step of 6.7 kPa. The red line is the calculated displacement by Stokes drag force for increasing shear modulus.

Shear wave imaging is based on estimating the elasticity of tissue by detecting the generated shear waves induced by ultrasound radiation force. The shear wave velocities detected are used to estimate the elastic properties of the tissue. The technique is considered to be good at distinguishing between a benign and malignant tumour in a breast. However, with the result in figure 5.17, it tends to be difficult to distinguish between the tumour types. After the shear modulus is around $\sim$ 5 kPa the behaviour of the breast tissue has minor variations for increasing values of shear modulus.

In figure 5.18, it is seen how the displacement pulses are shifted in time, due to increased values of shear modulus. Stiffer tissue increases the shear wave velocity c_{s}. $T_{\mathrm{s}} = R_{\mathrm{s}}/c_{\mathrm{s}}$, the period of shear displacement before reaching stationary solution, will therefore decrease with increasing c_{s}. Stiffer tissue decreases the displacement fluctuation and becomes more difficult to detect.

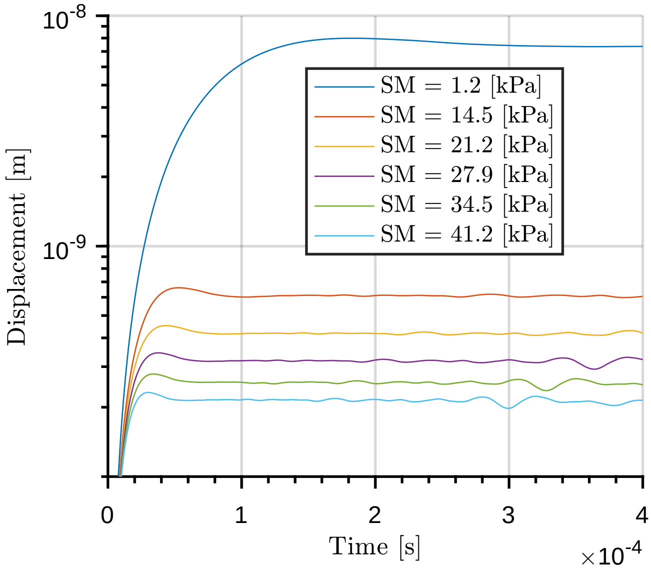

Figure 5.18: The stationary displacements of a microcalcification when the shear modulus of the surrounding tissue is varied. Time shifting due to increased shear wave velocity is observed.

5.3.2 Varying the weight of the microcalcification

To evaluate the potential effect of the density of the microcalcification in a stationary simulation the weight of the particle is varied. In figure 5.19 this resulted in a minor impact with a radiation force constantly applied to the microcalcification domain. As an agreement to Stokes drag force already is found, and the stationary displacement given by Stokes is unaffected by the density of the microcalcification, the result is as expected. The findings in section 5.1 conclude the microcalcification to be insufficient compared to the tissue in the induced displacement, which applies for varied densities of the microcalcification as well.

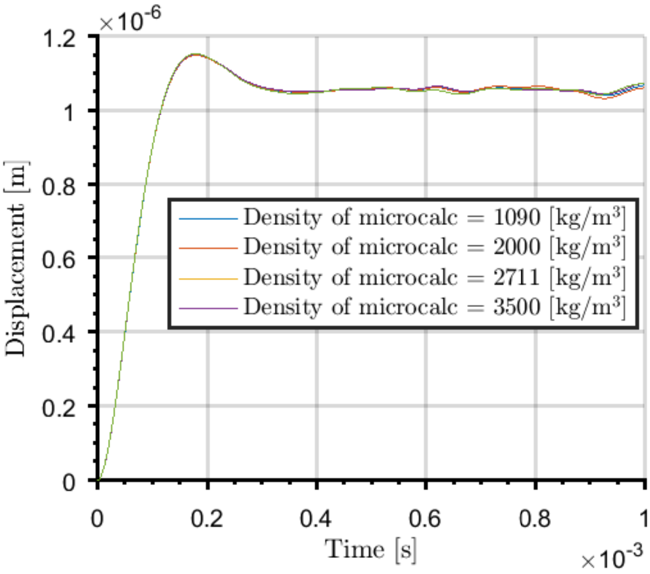

Figure 5.19: The stationary displacements of a microcalcification by varying the weight of the particle.

5.4 Experiments

Experiments were performed at the lab at ISB, NTNU. In experiments on the Twinkling Sign Artifact, both Color Flow and B-flow imaging were tested, but with Color Flow it was almost impossible to discover any twinkling at all. B-flow mode detected the microcalcification showing the particles as grey dots superimposed on a B-mode image of the surrounding tissue, as seen in figure 5.20.

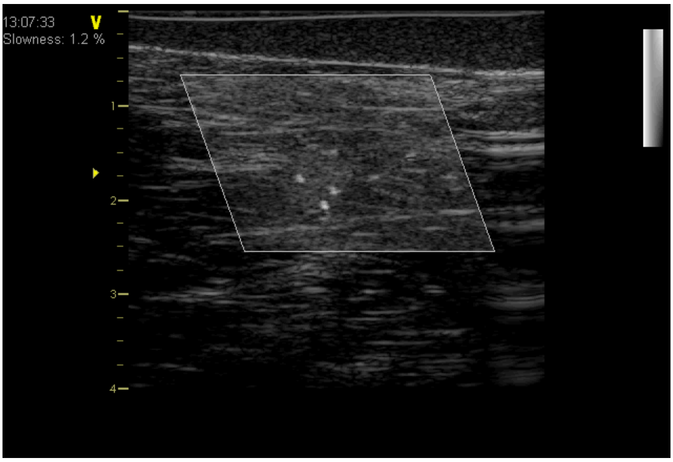

Figure 5.20: B-flow imaging mode detected three microcalcifications in the breast phantom in January 2018.

The experiment on B-flow twinkling was first performed in January 2018. However, in May 2018 it was discovered that the SURF scanner no longer detected the microcalcifications in the same breast phantom as earlier. Therefore, the B-flow twinkling experiment was performed again. The best imaging from this experiment is in figure 5.21, where only one of the three microcalcifications from figure 5.20 is detected. The probe was rotated 180°, such that the image in figure 5.21 is rotated compared to in figure 5.20. It was much more difficult finding a result as good as in figure 5.20 in these experiments. The same imaging mode (Carotid) with the same focus depth and the same 9L linear probe with a centre frequency of 8 MHz and PRF of 5 kHz described in section 3.1.2 were used.

Figure 5.22 shows the previous detection with SURF imaging as in[9]. During this thesis, detection with a SURF scanner like in figure 5.22 has not been possible to produce, none of the microcalcifications is detected. If radiation force is the triggering factor of SURF detection as well as B-flow twinkling by oscillating the microcalcifications, it should be easier to reproduce the experiments. Microbubbles of air in a crevice or on the surface of a microcalcification are possibly altered or disappeared, such that both twinkling and SURF detection are difficult to reproduce.

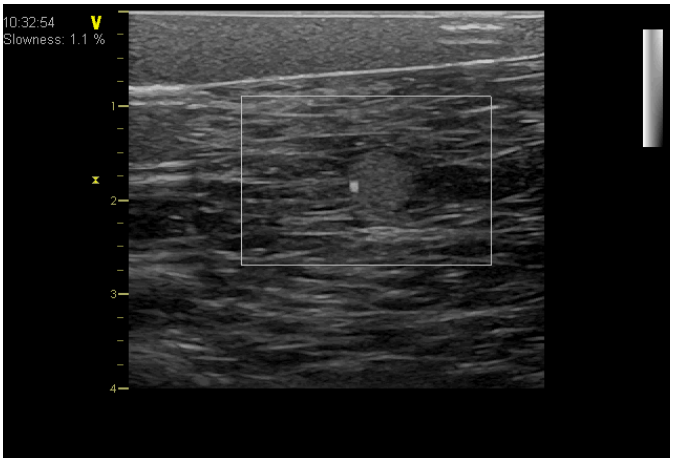
10:32:54
V
Slowness: 1.1 %
1
2
3
4

Figure 5.21: The B-flow twinkling experiment from May 2018 detected only one microcalcification.

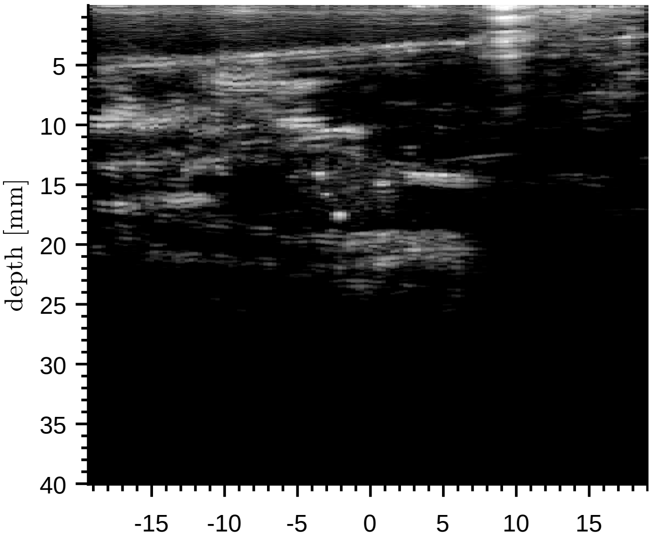
depth [mm]
5
10
15
20
25
30
35
40
-15
-10
-5
0
5
10
15

Figure 5.22: Previous SURF detection of microcalcifications as in [9], where the three microcalcifications are detected.

5.5 Discussion

This section is provided to summarise and structure the most important discussions in the analysis. First, the displacement of a microcalcification induced by radiation force from a SURF pulse is shown to be on a small scale, as small as in $\sim$ nm. Such a small displacement is difficult to detect with a SURF scanner. Simulations of homogeneous breast tissue compared to a tissue with a microcalcification embedded showed the tissue displacement to be the dominant factor of displacement. Compared to the size of the surrounding tissue, the microcalcification is too small to be prominent in the displacement even though its material properties are heavier and stiffer. Both SURF detection and B-flow imaging is based on detecting differences in an image. The dominance of the surrounding tissue tells that the radiation force-induced displacement of a microcalcification is not the triggering factor of SURF detection and the B-flow twinkling of microcalcifications. By using a narrow Gaussian force profile a minor difference in homogeneous breast tissue is noticed. Breast tissue is explained as a mass-spring system. Larger radial and vertical dimensions of radiation force applied trigger more mass of the breast tissue contribute to the shear displacement and expand the duration of shear displacement. The effect was observed when comparing displacement induced by a narrow Gaussian which is small in radial and vertical dimensions, such that the duration of displacement was shorter than for a SURF pulse. Radiation force from scattering is shown to be of minor importance and is not considered to be a possible reason for SURF detection of microcalcifications. This occurs as well due to the tissue and microcalcification relations in sizes.

By simulating several SURF pulses transmitted it is visualised the tissue pushing and further accelerating the microcalcification from behind. The contribution to displacement from a LF pulse is shown to be ~ 3 times smaller in magnitude compared to a HF pulse, even though the pulse period is five times longer. In existing studies[17], an oscillating behaviour of a microcalcification was not observed in experiments but suggested as a triggering factor of Twinkling Sign. With a PRF of $\approx 5000\,\mathrm{Hz}$, the microcalcification was shown to oscillate in simulations when focusing the radiation force on the microcalcification domain only. Achieving oscillations in experiments demand a narrow ultrasound pulse transmitted on the microcalcification only, which is unrealistic.

Applying a force constantly on the microcalcification domain only has proven an agreement with the Stokes drag force, which gives a relation between the displacement amplitude, radiation force, microcalcification radius and the stiffness of the surrounding tissue. These relations increases the physical insight of breast tissue under ultrasound transmission, the relation to Stokes drag force is not introduced in existing literature. The findings tell that it is difficult to distinguish between a malignant and a benign tumor in a breast with shear wave imaging. After the shear modulus is around the value of $\sim 5\,\mathrm{kPa}$, the behaviour of the tissue has minor variations with increasing shear stiffness. Stiffer tissue decreases the displacement fluctuation and becomes more difficult to detect.

Experiments on the breast phantom during this thesis have proven it difficult to reproduce the previous detection of microcalcifications. Detection of microcalcifications with SURF imaging is no longer possible. Producing twinkling with B-flow mode on a GE

Vivid E9-2 ultrasound scanner was much harder in May than in January, in January the twinkling was prominent. If the radiation force induced by an ultrasound pulse triggers both SURF detection and the twinkling in B-flow, the experiments should be reproducible. The radiation force to not be the triggering factor agrees with the displacement simulations. The findings in both simulations and experiments lead to microbubbles in a crevice or on the surface of a microcalcification, to be the main hypothesis for SURF detection. The same hypothesis applies to the Twinkling Sign Artifact as well. The experiments may have been difficult to reproduce if the bubbles have altered or disappeared.

Equation 2.58 gives the resonance frequency for a bubble in a free-space oscillation. SURF detection of microcalcifications has been achieved for a combined LF and HF pulse, and not with a HF pulse separately. Therefore, an interesting hypothesis is that the LF pulse oscillates a microbubble on the surface of a microcalcification making it detectable by the HF pulse. If the resonance frequency in equation 2.58 $f_{\mathrm{m}} \approx f_{\mathrm{LF}}$, this may be the situation, before the HF pulse detects. The polymetric gas constant for air is used in the calculations, $\gamma = 1.40$, the microbubbles in the breast phantom are considered to be air bubbles. The density used for the tissue is $\rho = 1090\,\mathrm{kg/m^3}$ and $p_{\mathrm{g0}} = 101\,\mathrm{kPa}$ is the atmosphere pressure. In figure 5.23 the resonance frequency is calculated for microbubbles with radius in the range 1 µm to 10 µm. For a microbubble of radius 4 mm the resonance frequency $f_{\mathrm{m}} = f_{\mathrm{LF}} = 0.8\,\mathrm{MHz}$. It is considered that the microbubbles with sizes such that the resonance frequency is in the range $f_{\mathrm{m}} \approx 0.6\,\mathrm{MHz}$ to 1 MHz can be oscillated by the LF pulse. Then the hypothesis holds for microbubbles with radius in the range $a \approx 3$ µm to 5 µm. A microcalcification will appear as a rigid boundary in this context.

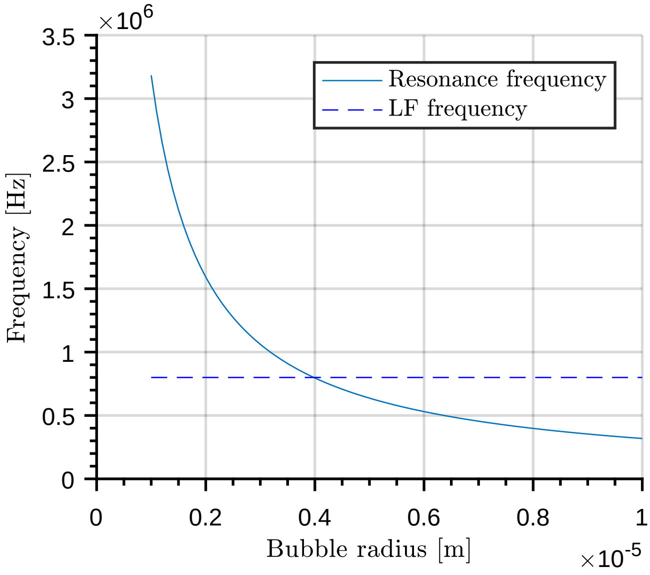

Figure 5.23: Calculated resonance frequency for microbubbles of air with radius of 1 µm to 10 µm and the dotted line is the LF frequency.

Chapter 6

Conclusion and suggestion of further work

The work done in this thesis has given physical insight of the shear displacement of a microcalcification embedded in breast tissue. First, the FEM-simulations in COMSOL have shown that the radiation force-induced displacement of a microcalcification is not the triggering factor of SURF detection. Displacement simulations of breast tissue with a microcalcification embedded and homogeneous breast tissue has been compared to provide the conclusion. Secondly, stationary simulations in this thesis have shown an agreement to the Stokes drag force, a relation that is not earlier introduced. With this, a deeper understanding of the physical parameters of a breast tissue is achieved.

The breast tissue modelled in COMSOL could have been modelled as a nonlinear elastic material, which is a realistic behaviour of breast tissue. However, finding correct material parameters would then have been more difficult and risky, as reference stress, reference strain and stress exponent are required in such a model in COMSOL. Modelling the breast tissue as the linear elastic material node was sufficient to discuss ultrasound radiation force-induced displacement as the triggering factor of SURF detection of microcalcifications. The viscous component of the shear visco-elasticity of tissue is not included in the model, but in reality, the displacement-amplitude will be limited by both this and radiation losses. To expand the model to include viscosity of the tissue the materials relaxation data is needed. Except limiting the amplitude of the displacements, expanding the model to include viscosity would not provide any change in the findings.

Microbubbles of air on the surface or in a crevice of a microcalcification as the triggering factor are suggested as the main hypothesis for SURF detection. Images from experiments on both B-flow twinkling and SURF detection contribute to this hypothesis, as earlier detection has been difficult or impossible to reproduce. The bubbles may have altered or disappeared. Calculations showing demands to the microbubble size, such that the resonance frequency of an oscillating bubble in free-space is close to the LF frequency are presented. The microcalcifications are not detected by a HF pulse separately. The effect of combining the HF pulse with a LF pulse may be an oscillating behaviour of the bubbles induced by the LF pulse. After that, the co-propagating HF pulse detects the oscillations.

6.1 Further work

The linear elastic model can be expanded to a nonlinear displacement model in COMSOL. Stress and strain parameters for breast tissue are required in such a model.

Radiation losses and shear visco-elasticity of tissue will in reality limit the displacement amplitude of a microcalcification. To complete the physical insight of breast tissue under ultrasound radiation force presented in this thesis these two factors should be addressed.

Experiments on the newly introduced nonlinear shear modulus of the breast phantom under uniaxial compression could be of interest. This is more relevant for larger induced displacements than by the SURF pulse used in this thesis.

Microbubbles with a radius of 3 µm to 5 µm in a crevice or on the surface of a microcalcification is suggested as the primary hypothesis to SURF detection of microcalcifications, and should be further investigated. A problem in studies of the bubbles earlier is that the bubbles are yet to be observed in a breast. In earlier research on the twinkling sign artifact microbubbles are investigated by experiments in a water tank. Displacement simulations as in this thesis of the microbubbles on the surface of a microcalcification in COMSOL is considered severe. The Solid Mechanics node is not sufficient to describe the behaviour of a microbubble.

Bibliography

[1] Karen Todd Lane and Helena R. Chang. *Breast cancer risk factors and prevention*. In Alberto Manetto, editor, Cancer Prevention And Early Diagnosis In Women, chapter 3, pages 48–68. Mosby, Elsevier Science, Philadelphia, Pennsylvania, 1st edition, 2004.

[2] Mammography National Cancer Institute, USA. `https://medlineplus.gov/mammography.html`, 2017. Accessed on 05.05.2018.

[3] Carla H. Van Gils, Johannes D. M. Otten, André L. M. Verbeek, Jan H. C. L. Hendriks, and Roland Holland. *Effect of mammographic breast density on breast cancer screening performance: a study in Nijmegen, the Netherlands*. Journal of Epidemiology and Community Health, 52(4): 267–271, 1998.

[4] J. M. Johnson, R. R. Dalton, S. M. Wester, J. Landercasper, and P. J.Lambert. *Histological correlation of microcalcifications in breast biopsyspecimens*. Archives of Surgery, vol. 134, no. 7, pp. 712–716, 1999.

[5] Martin E. Anderson, Mary S. Soo, Rex C. Bentley, and Gregg E. Trahey. *The detection of breast microcalcifications with medical ultrasound*. The Journal of the Acoustical Society of America, 101(1):29–39, 1997.

[6] S. Bahramian and M. F. Insana. *Improved microcalcification detectionin breast ultrasound: Phantom studies*. IEEE InternationalUltrasonics Symposium, 2014.

[7] Adriana Gregory, Mohammad Mehrmohammadi, Max Denis, and Azra Alizad. *Effect of Calcifications on Breast Ultrasound Shear Wave Elastography: An Investigational Study*. Researchgate, 2015.

[8] Bjørn A. J. Angelsen and Thor Andreas Tangen. *Nonlinear imaging with dual band pulse complexes*. SURF Technology AS, 2012.

[9] Even Flørenæs. *Estimation of nonlinear scattering for improved detection of micro calcifications for diagnosis of breast cancer using dual band ultrasound*. Master thesis, Norwegian University of Science and Technology, 2017.

[10] Chiao RY. *B-mode blood flow (B-flow) imaging*. Ultrason Symp 2000 IEEE, 2000.

[11] Brunese L, Romeo A, Iorio S, and et al. *A new marker for diagnosis of thyroid papillary caner*. J Ultras Med, 2008.

[12] Rahmouni A, Bargoin R, Herment A, and et al. *Color Doppler twinkling artifact in hyperechoic regions*. Radiology, 1996.

[13] Dr Ian Bickle and Dr Saeed Soltany Hosn. Twinkle artifact. `https://radiopaedia.org/articles/twinkle-artifact-1`. Accessed on 20.04.2018.

[14] Lei Liu, Kenichi Funamoto, Kei Ozawa, Makoto Ohta, Toshiyuki Hayase, and Masafumi Ogasawara. *In vitro study of ultrasound radiation force-driven twinkling sign using PVA-H gel and glass beads tissue-mimicking phantom*. Journal of Medical Ultrasonics, 2013.

[15] Jeong hwa Yang, Gwansuk Kang, and Min Joo Choi. *The role of the acoustic radiation force in color Doppler twinkling artifacts*. Ultrasonography, 2015.

[16] Julianna C Simon, Oleg A Sapozhnikov, Wayne Kreider, Michael Breshock1, James C Williams Jr, and Michael R Bailey. *The role of trapped bubbles in kidney stone detection with the color Doppler ultrasound twinkling artifact*. IPM, 2017.

[17] D. B. Leonov, N.S. Kullberg, A. I. Gromov, S. P. Morozov, and S. Yu. Kim. *Causes of Ultrasound Doppler Twinkling Artifact*. Acoustical Physics, 2018.

[18] Ulrik Fallrø. *Estimation of radiation force induced from a SURF pulse on a microcalcification particle*. Project thesis, Norwegian University of Science and Technology, 2017.

[19] The Editors of Encyclopaedia Britannica. Shear modulus. `https://www.britannica.com/science/shear-modulus`, 1998. Accessed on 20.04.2018.

[20] Wikipedia. Shear modulus. `https://en.wikipedia.org/wiki/Shear_modulus`, 2018. Accessed on 25.04.2018.

[21] The Editors of Encyclopaedia Britannica. Bulk modulus. `https://www.britannica.com/science/bulk-modulus`, 1998. Accessed on 20.04.2018.

[22] Wikipedia. Bulk modulus. `https://en.wikipedia.org/wiki/Bulk_modulus`, 2018. Accessed on 25.04.2018.

[23] Wikipedia. Poisson’s ratio. `https://en.wikipedia.org/wiki/Poisson%27s_ratio`, 2018. Accessed on 25.04.2018.

[24] B A J Angelsen. *Ultrasound Imaging - Waves, Signals and Signal Processing*. Emantec AS, Bugges veg 4B, 7051 Trondheim, Norway, December 2000.

[25] Ole Martin Brende. *Reverberation suppression with dual band imaging in medical ultrasound.* PhD thesis, Norwegian University of Science and Technology, 2016.

[26] Ola Finneng Myhre. *Dual-frequency Transducers for Ultrasound Imaging and Therapy.* PhD thesis, Norwegian University of Science and Technology, 2017.

[27] Bjørn A J Angelsen. *Ultrasound radiation force on a sub-cellular scale.* Department of Circulation and Medical Imaging, NTNU, 2017.

[28] Bjørn Angelsen. *Shear displacement of $CaCO_3$ particle in soft tissue.* SURF technology AS, Trondheim, 2018.

[29] Oleg A. Sapozhnikov and Michael R. Bailey. *Radiation force of an arbitrary acoustic beam on an elastic sphere in a fluid.* Department of Acoustics, Physics Faculty, Moscow State University, Leninskie Gory, Moscow 119992, Russia, 2013.

[30] Henrik Bruus. *Acoustic Radiation Force on Small Particles.* chapter 4, page 574. The Royal Society of Chemistry, Cambridge, United Kingdom, 1st edition, 2015.

[31] K. Yosioka, Y. Kawasima, and H. Hirano. *Acoustic radiation pressure on bubbles and their logarithmic decrement.* Acustica, 1955.

[32] Alon Grinenko. How to compute the acoustic radiation force. `https://www.comsol.com/blogs/how-to-compute-the-acoustic-radiation-force/`, 2015. Accessed on 31.05.2018.

[33] Wikipedia. Acoustic tweezers. `https://en.wikipedia.org/wiki/Acoustic_tweezers`, 2017. Accessed on 15.12.2017.

[34] Helmholtz decomposition. `https://en.wikipedia.org/wiki/Helmholtz_decomposition`, 2018. Accessed on 15.03.2018.

[35] Flow past a sphere ii: Stokes' law, the bernoulli equation, turbulence, boundary layers, flow separation, 2006.

[36] Miguel Bernal, Foucauld Chamming's, Mathieu Couade, Jeremy Bercoff, Mickaël Tanter, and Jean-Luc Gennisson. *In Vivo Quantification of the Nonlinear Shear Modulus in Breast Lesions: Feasibility Study.* IEEE TRANSACTIONS ON ULTRASONICS, FERROELECTRICS, AND FREQUENCY CONTROL, VOL. 63, NO. 1, 2016.

[37] Wikipedia. Rayleigh–plesset equation. `https://en.wikipedia.org/wiki/Rayleigh%E2%80%93Plesset_equation`, 2018. Accessed on 20.05.2018.

[38] Ola Finneng Myhre. Trial lecture: Sonoporation in cancer therapy, 2017.

[39] Providan MEDICAL EQUIPMENT. Ge vivid e9 for sale. `https://www.providianmedical.com/ultrasound-machines/ge/ge-vivid-e9/`, 2018. Accessed on 12.05.2018.

[40] GE Healthcare. Transducer guide logiq s7. `https://www3.gehealthcare.com/~/media/documents/us-global/products/ultrasound/transducer%20files/transducers/gehealthcare_logiq-s7_transducer-guide.pdf`, 2012.

[41] CIRS Tissue Simulation and Phantom Technology. Multi-modality breast biopsy and sonographic trainer. `http://www.cirsinc.com/products/all/105/multi-modality-breast-biopsy-and-sonographic-trainer/`, 2018. Accessed on 27.04.2018.

[42] iel. Multi-modality breast biopsy and sonographic trainer 073. `https://imagingequipment.co.uk/products/multi-modality-breast-biopsy-and-sonographic-trainer-073/`, 2018. Accessed on 29.05.2018.

[43] Johannes Kvam. *Fast simulation of surf ultrasound transmit pulse complexes using heterogeneous computing platforms.* Master's thesis, Norwegian University of Science and Technology, 2012.

[44] COMSOL. *COMSOL Documentation.* COMSOL, 1998-2017.

[45] KORTH KRISTALLE GMBH. Calcite ($caco_3$). `http://www.korth.de/index.php/162/items/11.html`. Accessed on 05.02.2018.

[46] Henrik Sönnerlind. Modelling linear elastic materials - how difficult can it be=. `https://www.comsol.com/blogs/modeling-linear-elastic-materials-how-difficult-can-it-be/`, 2015. Accessed on 29.01.2018.

[47] COMSOL. Using symmetries in comsol multiphysics. `https://www.comsol.com/support/knowledgebase/1038/`. Accessed on 21.05.2018.

[48] multiphysics CYCLOPEDIA. Finite element analysis (fea) software. `https://www.comsol.com/multiphysics/fea-software`. Accessed on 27.04.2018.

[49] COMSOL. Resolving time-dependent waves. `https://www.comsol.com/support/knowledgebase/1118/`. Accessed on 07.05.2018.

[50] Weija Lu and Bruno Haider. *Dominant factor analysis of b-flow twinkling sign with phantom and simulation data.* J Med Ultrasonics (2017) 44:37–50, 2017.

[51] The Korean Breast Elastography Study Group. *Practice guideline for the performance of breast ultrasound elastography.* Ultrasonography 2014;33:3-10, 2014.